

1        **A historical nutrient dataset (1895–2024) for the North Pacific:**  
2        **reconstructed from machine learning and hydrographic observations**

Chuanjun Du<sup>1\*</sup>, Naiwen Zheng<sup>1</sup>, Shuh-Ji Kao<sup>1</sup>, Minhan Dai<sup>2</sup>, Zhimian Cao<sup>2</sup>, Dalin Shi<sup>2</sup>, Qiancheng Li<sup>1</sup>, Hao Wang<sup>1</sup>, Xunlan Luo<sup>1</sup>, and Xiaolin Li<sup>2\*</sup>

<sup>1</sup>School of Marine Sciences, Hainan University, Haikou 570228, China

<sup>2</sup>State Key Laboratory of Marine Environmental Science, College of Ocean and Earth Sciences, Xiamen University, Xiamen 361102, China

Manuscript resubmitted to *Earth System Science Data*

**\*Corresponding Authors:** Chuanjun Du, [cjdu@hainanu.edu.cn](mailto:cjdu@hainanu.edu.cn); Xiaolin Li, [xlli@xmu.edu.cn](mailto:xlli@xmu.edu.cn)

3

4 **Key points:**

- 5 ● Rigorous data quality control procedures were applied to clean nutrient and  
6 hydrographic data collected from multiple sources in the North Pacific, following  
7 state-of-the-art practices.
- 8 ● Three machine learning models demonstrated low errors across diverse validation  
9 strategies.
- 10 ● We reconstructed a monumental database of ~473 million nutrient data points  
11 across 1.92 million stations (1895–2024), expanding the number of nutrient data  
12 points by a factor of 2,127–2,393 compared to original observations.

13

14

15 **Abstract**

16 Nutrients play a critical role in oceanic primary productivity and the biological pump.  
17 However, compared to hydrographic parameters such as temperature and salinity,  
18 nutrient observations are limited due to their labor-intensive and costly measurements.  
19 Thus, nutrient observations are several orders of magnitude sparser than hydrographic  
20 observations. In this study, we first established a rigorous data quality control procedure  
21 to clean the hydrographic and nutrient (including  $\text{NO}_3^-$ ,  $\text{NO}_2^-$ , DIP, and  $\text{Si}(\text{OH})_4$ )  
22 observations collected from World Ocean Database (WOD) and CLIVAR and Carbon  
23 Hydrographic Data Office (CCHDO) in the North Pacific. Subsequently, the cleaned  
24 and high-quality CCHDO dataset was used to train three machine learning models—  
25 Random Forest, Light Gradient Boosting Machine (LightGBM), and Gaussian Process  
26 Regression—to establish relationships between nutrient concentrations and key  
27 variables, including space coordinates (longitude, latitude, and depth), time variables  
28 (year and month), and water mass properties (indexed by potential temperature and  
29 salinity). Validation shows that the reconstruction closely matches the observations,  
30 with Root Mean Squared Errors (RMSEs) of  $<1.41$ ,  $<0.071$ ,  $<0.089$  and  $<3.07 \mu\text{mol}$   
31  $\text{kg}^{-1}$  for  $\text{NO}_3^-$ ,  $\text{NO}_2^-$ , DIP, and  $\text{Si}(\text{OH})_4$ , respectively. The validated models were then  
32 applied to reconstruct nutrient concentrations from the hydrographic observations in  
33 WOD, most of which lacked direct nutrient measurements. This resulted in  $\sim 473$   
34 million reconstructed nutrient data points across 1.92 million stations for each nutrient,  
35 spanning from 1895 to 2024, representing a 2,127 to 2,393-fold increase compared to  
36 the original nutrient observations in the North Pacific (197,539 to 222,234). This new  
37 dataset will be valuable for studying nutrient transport and budgets, spinning up and  
38 validating ocean biogeochemical models, assessing long-term nutrients and their  
39 stoichiometric changes driven by anthropogenic forcing and climate change. The  
40 dataset generated in this study is openly available on Zenodo at  
41 <https://zenodo.org/records/17451417>.

42

## 43 **1 Introduction**

44 Bio-essential elements such as nitrogen, phosphorus, and silicon constitute the  
45 fundamental material basis for marine ecosystems. Their concentrations govern  
46 primary and new production (e.g., Browning et al., 2023; Lipschultz et al., 2002; Moore  
47 et al., 2013) and subsequently regulate oceanic uptake of atmospheric CO<sub>2</sub> (Deutsch  
48 and Weber, 2012; Sigman and Hain, 2012). However, traditional nutrient data collection  
49 relies heavily on ship-based cruises and subsequent sample analysis, which are labor-  
50 intensive, inefficient, and costly (Du et al., 2021). Consequently, compared to the  
51 abundant hydrographic data collected from multiple platforms such as Conductivity-  
52 Temperature-Depth (CTD) and the Array for Real-time Geostrophic Oceanography  
53 (Argo) profilers, etc., nutrient observations are sparse in the ocean. These sparse  
54 nutrient observations limit our understanding of both small-scale and long-term nutrient  
55 variations and our comprehensive understanding of the mechanisms driving changes in  
56 oceanic production and ecosystem dynamics (Bidigare et al., 2009; Yasunaka et al.,  
57 2021; Karl et al., 2021).

58 To address this data sparsity, two main approaches have been commonly employed  
59 to augment the spatiotemporal coverage of the observed nutrient data. The first is  
60 objective analysis, which interpolates field measurements to generate broader spatial  
61 coverage, as implemented in products such as the World Ocean Atlas (WOA) (e.g.,  
62 Reagan et al., 2023; Lee et al., 2023). The second is data fusion, which establishes  
63 statistical relationships between nutrients and environmental predictors such as  
64 temperature (e.g., Kamykowski, 1987; Kamykowski et al., 2002; Kamykowski, 2008),  
65 density (e.g., Dugdale et al., 1989; Switzer et al., 2003), oxygen, salinity, and  
66 chlorophyll *a* (Goes et al., 1999; Palacios et al., 2013; Sarangi et al., 2011). Statistical  
67 methods including cubic regression, multiple linear regression (Steinhoff et al., 2010;  
68 Arteaga et al., 2015; Madani et al., 2024; Zhong et al., 2024), and generalized additive  
69 models (Palacios et al., 2013) are frequently used in these efforts.

70 Recent studies have demonstrated the potential of machine learning for enhancing  
71 the spatial and temporal coverage of nutrient data. For instance, Możejko and Gniot

72 (2008) used Artificial Neural Networks (ANNs) to model time series of total  
73 phosphorous concentrations in the Odra River. Self-organizing maps (SOMs) were used  
74 to estimate mixed layer nitrate and sea surface nutrients in the open ocean (Steinhoff et  
75 al., 2010; Yasunaka et al., 2014). Liu et al. (2022) applied Support Vector Regression,  
76 Random Forest Regression, and ANNs to reconstruct monthly surface nutrient  
77 concentrations in the Yellow and Bohai Seas from 2003 to 2019. Their results revealed  
78 pronounced seasonal and spatial variability in nutrient levels and underscored the  
79 influence of environmental drivers such as sea surface temperature and salinity.  
80 Similarly, Sundararaman and Shanmugam (2024) employed Gaussian Process  
81 Regression (GPR) models to estimate global ocean surface macronutrient  
82 concentrations using satellite-derived data, achieving high accuracy and demonstrating  
83 their suitability for large-scale marine ecosystem monitoring. Yang et al. (2024)  
84 employed a U-net and Earthformer to reconstruct the three-dimensional nitrate  
85 distribution by integrating surface data including wind speed, sea surface temperature,  
86 chlorophyll *a*, solar radiation, and precipitation in the Indian Ocean. These  
87 advancements highlight the expanding role of machine learning in marine biochemical  
88 data fusion and provide novel insights into nutrient dynamics and their ecological  
89 impacts.

90 However, many existing approaches rely solely on mathematical extrapolation or  
91 data fusion and often neglect the influence of physical seawater properties, such as  
92 water mass characteristics. Using the relationship between nutrient concentration and  
93 water masses (indexed by temperature and salinity), Du et al. (2021) successfully  
94 predicted the nutrient concentrations in the South China Sea. However, the water  
95 masses and their relationship with nutrients can also vary with space and time, which  
96 should also be taken into consideration. In addition, most research has predominantly  
97 focused on nutrient predictions at surface waters—driven by readily available remote-  
98 sensing measurements of sea surface temperature and chlorophyll *a*—while subsurface  
99 nutrient distributions remain poorly studied.

100 The North Pacific Ocean is one of the largest marine biomes in the global ocean (Karl  
101 and Church, 2017), spanning a broader longitudinal range than the other oceans in the  
102 world and a latitudinal range from tropical to polar regions. It includes a subtropical  
103 gyre characterized by extremely low surface nutrient concentrations due to Ekman  
104 convergence (e.g., Dave and Lozier, 2010; Browning et al., 2021; Dai et al., 2023), and  
105 subpolar gyres in the north with elevated nutrient concentrations driven by Ekman  
106 divergence. The atmospheric deposition (e.g., Martino et al., 2014; Qi et al., 2020), N<sub>2</sub>-  
107 fixation (e.g., Dai et al., 2023), and denitrification (Bonnet et al., 2017) are thought to  
108 the main nutrient sources and sinks, which are decoupled in space and time in the North  
109 Pacific. It has been reported that the North Pacific Subtropical Gyre (NPSG) plays an  
110 important role in fixed N inputs in summer, but also contributes disproportionately to  
111 losses due to intense water-column denitrification in the eastern Pacific low-oxygen  
112 zones (Eugster et al., 2012; Wang et al., 2019).

113 The North Pacific Ocean is influenced by multiple upwelling and current systems,  
114 including the equatorial and California upwelling systems, North Equatorial Current,  
115 Kuroshio Current, etc., which further change nutrient levels in these regions. In addition,  
116 the North Pacific Ocean exhibits abundant mesoscale eddies (Chelton et al., 2007),  
117 which play a critical role in redistributing nutrients and modulating biological activity  
118 (e.g., Benitez-Nelson et al., 2007; Ascani et al., 2013; Barone et al., 2022). The  
119 interaction of these multi-scale physical processes with biogeochemical processes  
120 results in highly dynamic nutrient variability in the upper ocean. Therefore, high-  
121 resolution and extensive nutrient datasets are essential to accurately resolve the nutrient  
122 dynamics. Although the WOA (Reagan et al., 2023) serves as a primary nutrient  
123 database and is widely used for boundary conditions in biogeochemical models, its  
124 applicability is constrained by relatively coarse spatial resolution (currently 1°) and  
125 climatological smoothing, which limit its ability to represent mesoscale and episodic  
126 features or to capture long-term variations.

127 In the North Pacific, Yasunaka et al. (2014) used the SOMs technique to generate  
128 monthly surface nutrient maps by integrating sea surface temperature, salinity,

129 chlorophyll *a*, and mixed layer depth. These maps revealed seasonal and interannual  
130 variability in surface nutrient distributions in the northern North Pacific. To investigate  
131 long-term changes, Yasunaka et al. (2016) applied Optimal Interpolation to analyze the  
132 spatial and temporal evolution of surface nutrient concentrations. Lee et al. (2023)  
133 provided spatiotemporally gridded nitrate and phosphate data in northwest Pacific from  
134 1980 to 2019 using the spatiotemporal kriging technique. Wang et al. (2023) used the  
135 deep neural network model to estimate nitrate concentrations in the upper northwestern  
136 Pacific Ocean using temperature and salinity as the primary input parameters.

137 In this study, we first collected nutrient data from public databases and applied  
138 rigorous quality control procedures. Using machine learning methods, we established  
139 relationships between nutrient concentrations and water mass properties, spatial  
140 coordinates, and temporal variables. We then evaluated the model performance through  
141 a comprehensive error analysis. Finally, the validated models were applied to  
142 reconstruct historical nutrient distributions across the North Pacific from 1895 to 2024.

## 143 **2 Data and Methods**

### 144 **2.1 Observation data**

145 Field observations were originally downloaded from the Climate and Ocean:  
146 Variability, Predictability, and Change (CLIVAR) and Carbon Hydrographic Data  
147 Office (CCHDO), which distributes vessel-based hydrographic data from programs  
148 such as the World Ocean Circulation Experiment (WOCE), Joint Global Ocean Flux  
149 Study (JGOFS), GO-SHIP, CLIVAR, and other repeat hydrography efforts  
150 (<https://cchdo.ucsd.edu/>). In total, 631 cruises were collected in the North Pacific,  
151 comprising 228,091, 197,617, 225,403, and 212,660 data points for  $\text{NO}_3^- + \text{NO}_2^-$   
152 ( $\text{NO}_x^-$ ),  $\text{NO}_2^-$ , DIP, and  $\text{Si}(\text{OH})_4$ , respectively (Table 1). The dataset spans from 1973  
153 to 2022 and was downloaded on October 1 2024; any updates made after this date were  
154 not included in this study. The data cover a geographic range from 120.08°E to 95.17°W  
155 and from 2.05°S to 60.25°N. The study domain was slightly extended into the South  
156 Pacific to mitigate potential boundary effects during model development.

157 Table 1. Information on nutrients and their associated hydrographic data collected  
 158 from CLIVAR and Carbon Hydrographic Data Office (CCHDO) and the data  
 159 information after quality control (QC).

	Original data information		Data information after QC	
	Data	Stations	Data	Stations
Temperature	327792	15127	327688	15125
Salinity	328502	15274	328275	15269
NO <sub>x</sub> <sup>-</sup>	217725	9588	213962	9021
NO <sub>2</sub> <sup>-</sup>	197617	8233	197539	8228
DIP	225403	9623	222234	9474
Si(OH) <sub>4</sub>	212660	8220	210447	8121

160 Hydrographic data for nutrient reconstruction were obtained from the World Ocean  
 161 Database (WOD; Mishonov et al., 2024), which compiles observations from various  
 162 platforms, including Autonomous Pinniped Bathythermograph (APB), Conductivity-  
 163 Temperature-Depth profiler (CTD), Drifting Buoy (DRB), Glider (GLD), Mechanical  
 164 Bathythermograph (MBT), Moored Buoy (MRB), Ocean Station Data (OSD), Profiling  
 165 Float (PFL), and Undulating Oceanographic Recorder (UOR). Since nutrient  
 166 reconstruction models rely on relationships with water masses, only samples containing  
 167 both temperature and salinity measurements were used; therefore, most APB  
 168 observations, which record only temperature, were excluded. Among these platforms,  
 169 CTD, OSD, and PFL provided the majority of usable data. Additionally, several  
 170 marginal seas—including the South China Sea, the Yellow Sea, the Sea of Japan, and  
 171 the Sea of Okhotsk—were excluded from this study because they are semi-enclosed  
 172 and strongly influenced by terrestrial inputs. The spatial domain was consistent with  
 173 that used for the CCHDO dataset, while the temporal coverage extended from 1875 to  
 174 2024. In total, 577,215,683 data points from 2,284,448 stations across 40,113 original  
 175 cruises were collected (Table 2). In addition, the OSD data before 1970 were extracted  
 176 for nutrient validation in section 3.1. A total of 102,424, 125,142, 447,335, and 294,734  
 177 data points were collected for NO<sub>3</sub><sup>-</sup>, NO<sub>2</sub><sup>-</sup>, DIP, and Si(OH)<sub>4</sub>, respectively.

178 Table 2. Information on hydrographic data collected from World Ocean Database, and  
 179 the data information after quality control (QC). See main text for acronyms' full  
 180 name.

Platform	Original data information			Data information after QC		
	Data	Stations	Cruises	Data	Stations	Cruises
APB	692302	46454	189	543714	37209	154
CTD	157914052	315177	8785	135584007	297036	8415
GLD	119302218	288840	384	69834989	285778	380
OSD	8885341	592225	21169	6942902	505780	17671
PFL	284781001	700798	9511	255423345	680531	9099
UOR	3373799	26699	7	3304158	25813	6
MRB	1459032	293734	65	1019565	88487	19
DRB	807938	20521	3	0	0	0
Total	577215683	2284448	40113	472652680	1920634	35744

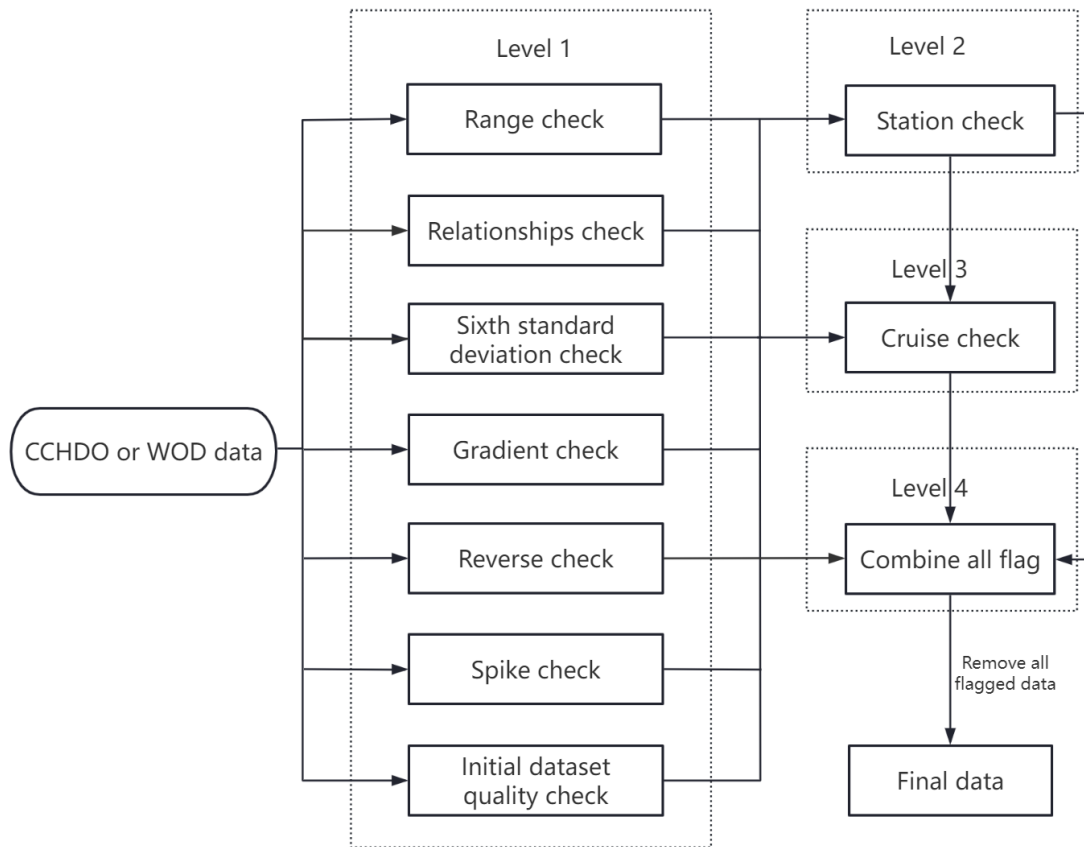
181

## 182 2.2 Data quality control

183 Given that the data were collected from multiple platforms using various methods  
 184 over a long-time span and broad spatial range, quality control (QC) was essential (Du  
 185 et al., 2021; Wang et al., 2025). Following the QC procedures developed by the World  
 186 Ocean Database (WOD) (Garcia et al., 2024), we applied comprehensive QC protocols  
 187 (Fig. 1) to both CCHDO and WOD datasets, including hydrographic and nutrient  
 188 variables.

189 Four levels of QC were applied to identify and remove potentially erroneous or low-  
 190 quality records from the CCHDO and WOD datasets. The first level targeted individual  
 191 measurements, including several checks. (1) A range check was conducted by defining  
 192 depth-dependent acceptable value ranges for each parameter; data falling outside these  
 193 ranges were flagged as invalid. This check was applied to temperature, salinity,  $\text{NO}_x^-$ ,  
 194  $\text{NO}_2^-$ , DIP, and  $\text{Si}(\text{OH})_4$ . Note that the  $\text{NO}_x^-$  denotes the sum concentration of  $\text{NO}_2^-$  and

195  $\text{NO}_3^-$ . At stations lacking direct  $\text{NO}_x^-$  measurements,  $\text{NO}_x^-$  concentrations were derived  
196 by summing discrete  $\text{NO}_2^-$  and  $\text{NO}_3^-$  observations. (2) An empirical relationship check  
197 was performed to verify consistency among paired variables based on predefined  
198 acceptable domains, including temperature–salinity, temperature– $\text{NO}_x^-$ , temperature–  
199  $\text{NO}_2^-$ , temperature–DIP, temperature– $\text{Si}(\text{OH})_4$ , salinity– $\text{NO}_x^-$ , salinity– $\text{NO}_2^-$ , salinity–  
200 DIP, salinity– $\text{Si}(\text{OH})_4$ ,  $\text{NO}_x^-$ –DIP, and  $\text{NO}_x^-$ – $\text{Si}(\text{OH})_4$ . (3) A six-standard-deviation  
201 check was conducted by calculating the mean and standard deviation at each depth level;  
202 values falling beyond six standard deviations were flagged as outliers. (4) A gradient  
203 check assessed the vertical gradients of each parameter at each depth level across  
204 stations; data showing abnormal gradients exceeding five standard deviations from the  
205 mean were flagged as questionable. (5) A depth/potential density ( $\sigma_\theta$ ) inversion check  
206 was applied to detect unrealistic reversals in parameters such as temperature and  
207 nutrients, which typically exhibit monotonic relationships with depth or  $\sigma_\theta$  in stratified  
208 waters; measurements violating preset thresholds for depth–temperature, depth– $\text{NO}_x^-$ ,  
209 depth–DIP, depth– $\text{Si}(\text{OH})_4$ ,  $\sigma_\theta$ –temperature,  $\sigma_\theta$ – $\text{NO}_x^-$ ,  $\sigma_\theta$ –DIP, and  $\sigma_\theta$ – $\text{Si}(\text{OH})_4$  were  
210 flagged. (6) A spike check was implemented to identify abrupt deviations (spikes)  
211 between a measurement and its adjacent vertical neighbors; if the difference exceeded  
212 a defined threshold, the data point was flagged as suspect. This check was applied to  
213 temperature,  $\text{NO}_x^-$ , DIP, and  $\text{Si}(\text{OH})_4$ . (7) Only measurements with an original quality  
214 flag of ‘good’ from CCHDO and WOD were retained, while those marked as  
215 questionable or erroneous were flagged as outliers.



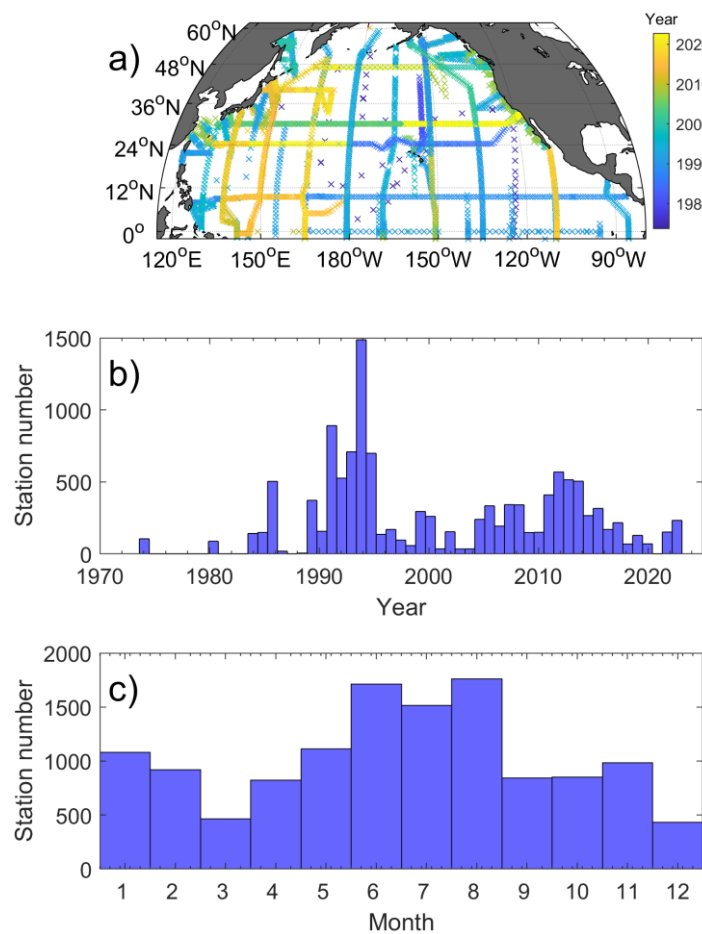
217

218 **Figure 1.** Data quality control procedures for temperature, salinity and nutrients  
 219 collected from the CLIVAR and Carbon Hydrographic Data Office (CCHDO) and the  
 220 World Ocean Database (WOD) datasets.

221

222 Building on the individual-level QC, we implemented additional QC at the station  
 223 and cruise levels. At the station level, if a station profile contained more than 20%  
 224 flagged data points, all data from that station were flagged as questionable. At the cruise  
 225 level, if over 30% of a cruise's data were flagged, all data from that cruise were flagged.  
 226 The final step integrated flags from all three levels (individual, station, and cruise), and  
 227 any data flagged at any level were excluded. This hierarchical QC protocol effectively  
 228 eliminates low-quality data. Although this approach may discard some high-quality  
 229 measurements, the large volume of available data necessitates strict QC to ensure  
 230 reliability.

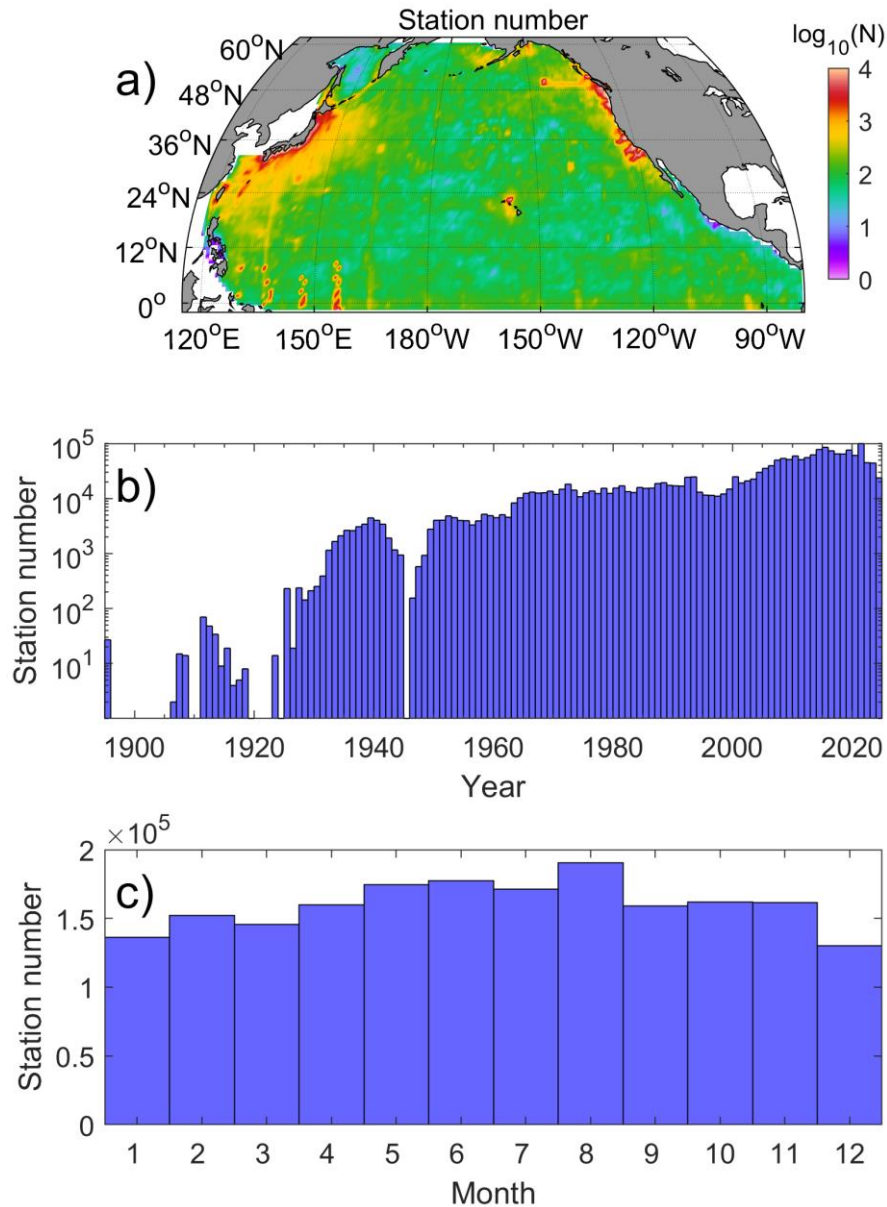
231 After quality control, the CCHDO dataset retained 214,943 (9,120), 197,539 (8,228),  
 232 222,234 (9,457) and 210,447 (8,123) data points (stations), accounting for 94.2%  
 233 (95.1%), 100.0% (99.9%), 98.6% (98.5%) and 99.0% (98.8%) of the original data  
 234 points (stations) for  $\text{NO}_x^-$ ,  $\text{NO}_2^-$ , DIP, and  $\text{Si}(\text{OH})_4$ , respectively (Table 1). The retained  
 235 stations cover nearly the entire North Pacific Ocean (Fig. 2a), spanning from 1972 to  
 236 2023. Most observations were collected after 1980, with a substantial increase after  
 237 1990 (Fig. 2b). Seasonally, the number of stations in June, July, and August was  
 238 approximately three times greater than that in March and December (Fig. 2c).



239  
 240 **Figure 2.** Spatial and temporal distributions of  $\text{NO}_x^-$  (nitrate plus nitrite) after quality  
 241 control in the North Pacific. a) Distribution of  $\text{NO}_x^-$  data locations, with points color-  
 242 coded by year; b) station counts per year; c) station counts per month.

243  
 244 Following quality control, the final WOD dataset comprised 472,652,680  
 245 temperature and salinity data points from 1,920,634 stations across 35,744 cruises,

246 spanning 1895 to 2024. These represent 81.9% of the original observations, 84.1% of  
247 the original stations, and 89.1% of the original cruises, respectively (Table 2). Spatially,  
248 station counts per  $1^\circ \times 1^\circ$  grid cell range from 1 to 31,851, with a mean of 249 stations  
249 per cell (Fig. 3a). High sampling densities are found off eastern Japan and western  
250 North America, resulting from high frequency observations from CTD and OSD  
251 platforms, whereas elevated counts in the southwestern North Pacific primarily result  
252 from MRB observations. Temporally, fewer than 300 stations per year were collected  
253 before 1930. The annual number of stations exceeds 10,000 after 1964 and peaked at  
254 approximately 100,000 in 2021 (Fig. 3b). Seasonally, station numbers are highest from  
255 May to August (Fig. 3c). Overall, the collected WOD dataset provides 2127–2393 times  
256 more observations and 202 times more station records than the CCHDO dataset.



257

258 **Figure 3.** Spatial and temporal distribution of the World Ocean Database (WOD) data  
 259 after quality control. a) Station counts per  $1^\circ \times 1^\circ$  grid cell; b) station counts per year;  
 260 c) station counts per month.

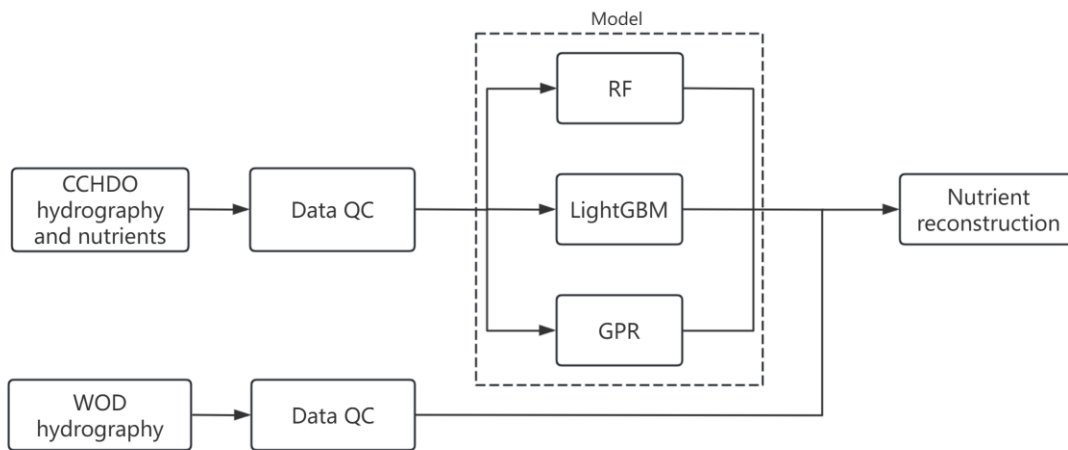
261

### 262 **2.3 Machine learning and nutrient reconstruction**

263 After rigorous data quality control, CCHDO data were used to train machine learning  
 264 models. Three algorithms including Random Forest (RF), Light Gradient Boosting  
 265 Machine (LightGBM), and Gaussian Process Regression (GPR) were applied to  
 266 establish the relationship between environmental parameters and nutrient

267 concentrations. These methods are widely used in marine science (Hu et al., 2021;  
268 Huang et al., 2022; Yu et al., 2022; Chen et al., 2023; Sundararaman and Shanmugam,  
269 2024). The use of diverse models helps decrease algorithm selection bias. RF is an  
270 ensemble technique based on bagging, which builds multiple independent decision  
271 trees and aggregates their outputs by voting or averaging (Liaw and Wiener, 2002). Its  
272 strengths include high predictive accuracy and reduced overfitting owing to the large  
273 number of trees. RF has been applied to predict global primary production (Huang et  
274 al., 2021), chlorophyll concentrations (Madani et al., 2024), nutrients (Chen et al., 2023;  
275 Chen et al., 2024), dissolved iron (Huang et al., 2022), surface ocean  $p\text{CO}_2$  (Chen et al.,  
276 2019), and  $\text{N}_2$  fixation rates (Yu et al., 2024).

277 LightGBM is an ensemble learning algorithm based on Gradient Boosting Decision  
278 Trees (GBDT). Compared to standard GBDT, LightGBM employs a leaf-wise tree  
279 growth strategy and a histogram-based binning technique to improve predictive  
280 accuracy and computational efficiency (Ke et al., 2017). It has been successfully  
281 applied to predict water levels (Gan et al., 2021), salinity (Dong et al., 2022; Wang et  
282 al., 2022), and chlorophyll  $a$  concentration (Su et al., 2021). GPR is a non-parametric  
283 Bayesian approach that infers relationships by defining a prior distribution over  
284 functions via kernel-based covariance matrices, rather than estimating fixed  
285 coefficients. This flexibility allows GPR to capture complex, nonlinear input–output  
286 relationships and to quantify prediction uncertainty. GPR has been used in  
287 oceanography to estimate global dissolved oxygen and nutrient concentrations  
288 (Sundararaman and Shanmugam, 2024).

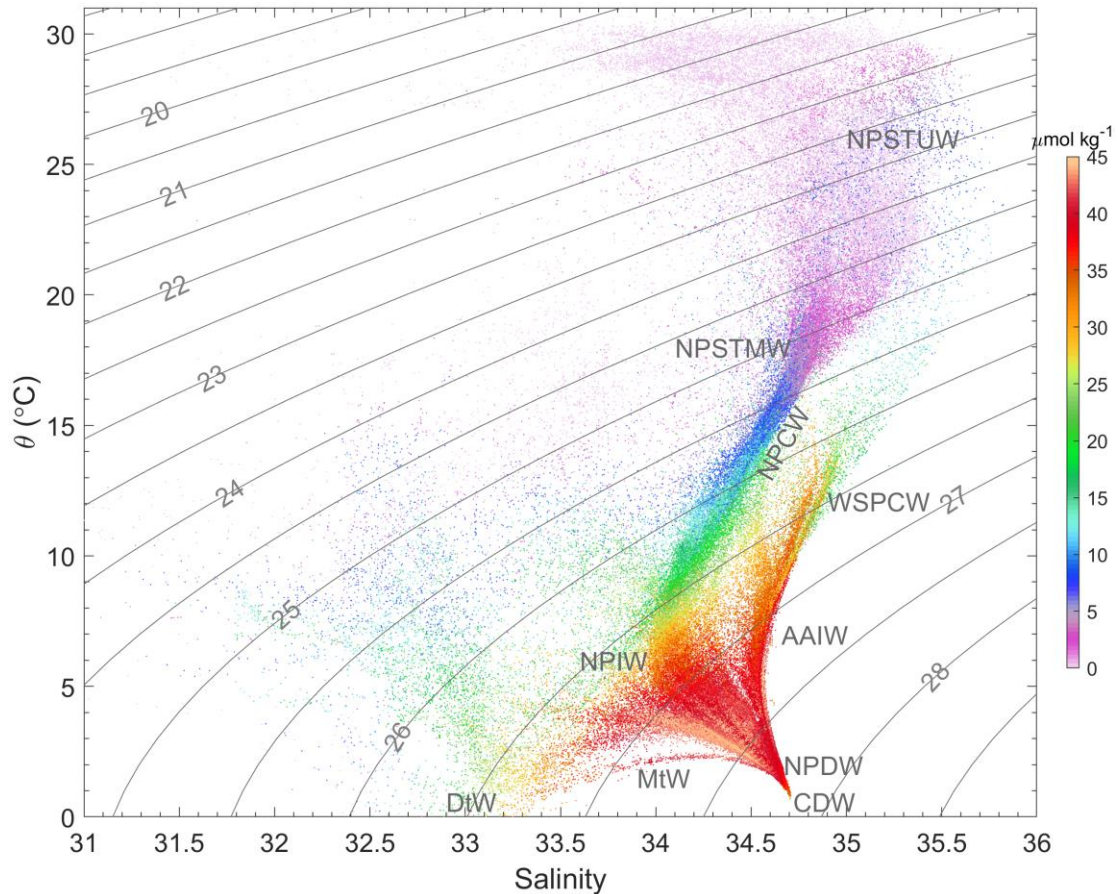


290

291 **Figure 4.** Flowchart of the machine learning framework and its application to WOD  
 292 hydrographic data for nutrient reconstruction.

293

294 In this study, we used spatial coordinates (longitude, latitude, depth), temporal  
 295 variables (month and year), and water mass properties (represented by potential  
 296 temperature and salinity) as environmental predictors of nutrient concentrations. The  
 297 time predictors used month and year with decimals to capture seasonal, interannual,  
 298 and long-term variability. The North Pacific contains distinct water masses, including  
 299 North Pacific Subtropical Water, North Pacific Intermediate Water, Antarctic  
 300 Intermediate Water, Western South Pacific Central Water, North Pacific Deep Water,  
 301 and Pacific Deep Water, as well as Circumpolar Deep Water (e.g., Talley et al., 2011;  
 302 Fuhr et al., 2021). These water masses mix to form different water types associated with  
 303 distinct nutrient concentrations (Fig. 5). Water types have been found to be an important  
 304 parameter to reconstruct nutrient concentrations in the South China Sea (Du et al., 2021).  
 305 Thus, potential temperature and salinity serve as proxies for water mass identification.



306

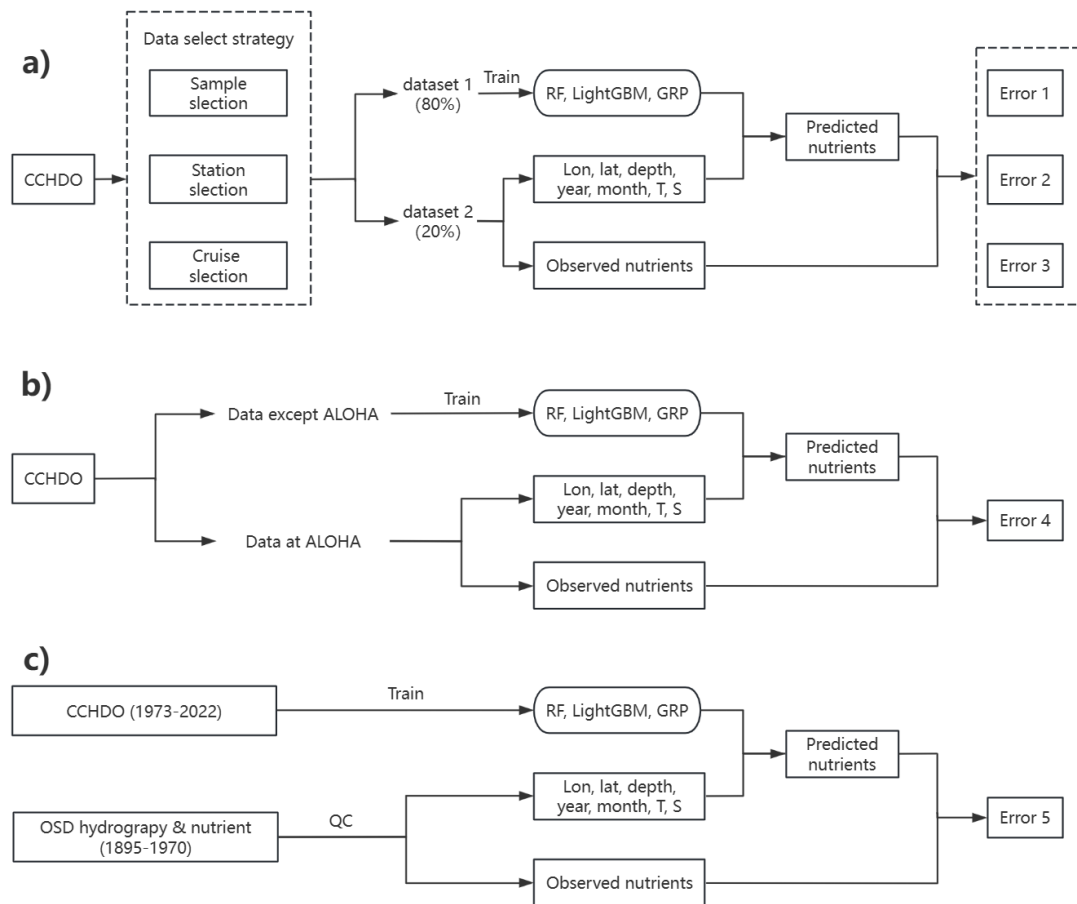
307 **Figure 5.** The water masses (indicated by salinity and potential temperature ( $\theta$ )) and  
 308  $\text{NO}_x^-$  ( $\text{NO}_3^- + \text{NO}_2^-$ ; color shading) relationships in the North Pacific. The temperature  
 309 and salinity data were collected from the CCHDO dataset. The gray contour lines and  
 310 number denote the potential density anomaly. The typical water masses are shown as  
 311 follows: North Pacific Central Water (NPCW), North Pacific Subtropical Underwater  
 312 (NPSTUW), North Pacific Subtropical Mode Water (NPSTMW), North Pacific  
 313 Intermediate Water (NPIW), Dichothermal Water (DtW), Mesothermal Water (MtW),  
 314 Antarctic Intermediate Water (AAIW), Western South Pacific Central Water (WSPCW),  
 315 Pacific Deep Water (PDW), and Circumpolar Deep Water (CDW). The water masses  
 316 and their acronyms are follow the classifications in Talley et al. (2011) and Fuhr et al.  
 317 (2021).

318

### 319 **3 Results**

#### 320 **3.1 Error estimation**

321 Leave-one-out cross-validation was primarily used to quantify model reconstruction  
322 errors. The CCHDO dataset was divided into training and testing subsets for model  
323 development and performance evaluation, respectively. To assess how data partitioning  
324 affects error metrics, we implemented four validation methods based on different data-  
325 selection strategies (Fig. 6a). The first three methods involved partitioning the CCHDO  
326 dataset into training (80%) and testing (20%) subsets. These methods employed three  
327 data selection strategies: (1) sample-random, by withholding 20% of individual samples;  
328 (2) station-random, by withholding 20% of stations; and (3) cruise-random, by  
329 withholding 20% of cruises. Predictions for the held-out subsets, generated using their  
330 respective spatial, temporal, and water mass property data, were compared against the  
331 actual withheld nutrient measurements to calculate error metrics. These partitioning  
332 strategies were designed to evaluate potential errors under the sparse and non-uniform  
333 spatiotemporal distribution of observations: Error 1 represented an optimistic estimate  
334 (validation data are likely colocated with training data in space and time), Error 3  
335 represented a conservative, generalized scenario (validation data are independent of  
336 training data), Error 2 provided an intermediate estimate (validation data may share  
337 spatial/temporal context with training data within the same cruise). The choice of error  
338 metric (Error 1, 2, or 3) should be guided by the degree of extrapolation in the intended  
339 application relative to the training data's spatiotemporal distribution.



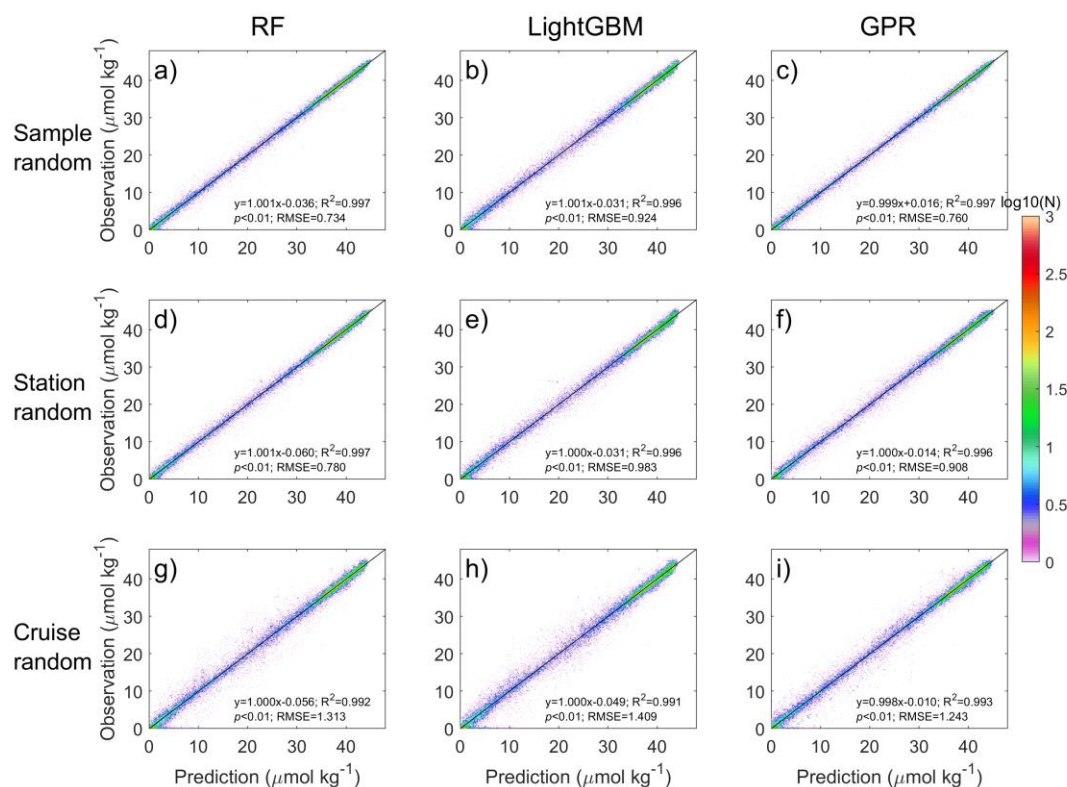
341

342 **Figure 6.** Schematic of the error estimation procedure. a) Error estimation based on  
 343 three types of data selection strategy; b) assessing temporal error evolution by  
 344 excluding the data at Station ALOHA; c) examining the models' reconstruction error  
 345 using the hydrographic and nutrient data before 1970. The T and S denote the potential  
 346 temperature and salinity, respectively.

347

348 The validation results for reconstructed  $\text{NO}_x^-$  versus observations under the first three  
 349 data-selection strategies are shown in Fig. 7. RF and GPR exhibited nearly identical  
 350 performance, with regression slopes of 0.992–0.998,  $R^2 > 0.992$ , and Root Mean  
 351 Squared Errors (RMSEs) between 0.734 and 1.313  $\mu\text{mol kg}^{-1}$  (Fig. 7a, c, d, f, g, i).  
 352 LightGBM showed slightly lower accuracy (slope: 0.991–0.995;  $R^2$ : 0.991–0.996;  
 353 RMSEs: 0.780–1.419  $\mu\text{mol kg}^{-1}$ ) (Fig. 7b, e, h). Across different data-selection  
 354 strategies, sample-random (Error 1) yielded the lowest errors (RMSEs: 0.734–0.983  
 355  $\mu\text{mol kg}^{-1}$ ) (Fig. 7a–c), station-random (Error 2) was intermediate (RMSEs: 0.908–  
 356 1.313  $\mu\text{mol kg}^{-1}$ ) (Fig. 7d–f), and cruise-random (Error 3) produced the highest errors

357 (RMSEs: 1.243–1.424  $\mu\text{mol kg}^{-1}$ ) (Fig. 7; Table 3). This gradient in error estimates  
 358 underscores the necessity of employing different data-selection strategies for a  
 359 comprehensive error assessment. The high slopes and  $R^2$  values ( $>0.99$ ) achieved across  
 360 all algorithms and data-selection strategies confirmed the robustness of the nutrient  
 361 reconstructions.



362  
 363 **Figure 7.** Validating the reconstructed  $\text{NO}_x^-$  concentrations using leave-one-out cross-  
 364 validation with different data selection strategies and machine learning methods. Plots  
 365 shown in row 1 correspond to the sample random strategy (a-c), row 2 correspond to  
 366 the station random strategy (d-e), and row 3 correspond to the cruise random  
 367 strategy (g-i). Plots shown in column 1 correspond to the Random Forest (RF; a, d, and  
 368 g), column 2 correspond to the LightGBM (b, e, and h), and column 3 correspond to  
 369 the Gaussian Process Regression (GPR; c, f, and i). The black lines and text show the  
 370 fitted linear regressions, regression equations, coefficient of determination ( $R^2$ ),  $p$   
 371 values, and Root Mean Squared Errors (RMSEs). The color represents the data density  
 372 ( $N$ , number of observations). Note that the logarithmic scale of  $N$  is applied.

373

374 Reconstruction errors for  $\text{NO}_2^-$ , DIP, and  $\text{Si}(\text{OH})_4$  are summarized in Figs. S1–S3  
 375 and Table 3. Across methods, the RMSEs were below 0.079  $\mu\text{mol kg}^{-1}$  for  $\text{NO}_2^-$ , 0.089

376  $\mu\text{mol kg}^{-1}$  for DIP, and  $3.07 \mu\text{mol kg}^{-1}$  for  $\text{Si}(\text{OH})_4$ . DIP and  $\text{Si}(\text{OH})_4$  exhibited similar  
 377 error trends: RMSEs increased from sample-random to station-random to cruise-  
 378 random selection. In contrast,  $\text{NO}_2^-$  reconstruction exhibited lower accuracy than  $\text{NO}_x^-$ ,  
 379 DIP, and  $\text{Si}(\text{OH})_4$ , with regression slopes of 0.48–0.68 and  $R^2$  values of 0.32–0.72. RF  
 380 and LightGBM outperform GPR for  $\text{NO}_2^-$ . The poorer  $\text{NO}_2^-$  performance likely reflects  
 381 its generally low concentrations (mostly  $<0.5 \mu\text{mol kg}^{-1}$ ) and high biological variability.  
 382 Thus, we highlight  $\text{NO}_2^-$  as a high-uncertainty reconstruction.

383 Table 3 The Root Mean Squared Errors of nutrient reconstruction from different error  
 384 evaluation strategies (unit:  $\mu\text{mol kg}^{-1}$ ).

Data selection strategy	$\text{NO}_x^-$			$\text{NO}_2^-$			DIP			$\text{Si}(\text{OH})_4$		
	RF	Light GBM	GPR	RF	Light GBM	GPR	RF	Light GBM	GPR	RF	Light GBM	GPR
Sample random	0.724	0.924	0.760	0.049	0.054	0.079	0.056	0.070	0.055	1.90	2.30	1.53
Station random	0.780	0.983	0.908	0.065	0.068	0.072	0.058	0.071	0.065	2.07	2.45	2.20
Cruise random	1.313	1.409	1.243	0.054	0.057	0.071	0.080	0.089	0.084	2.79	3.07	2.94
ALOHA validation	0.701	0.842	0.674	—	—	—	0.066	0.079	0.064	2.13	2.48	2.32

385

386 Understanding the spatiotemporal structure of reconstruction errors is also important  
 387 for assessing the models' reconstruction applicability. As shown in Figs. S4-S7, the  
 388 reconstruction errors of  $\text{NO}_3^-$ , DIP, and  $\text{Si}(\text{OH})_4$  are generally small in the surface layer,  
 389 increase with depth to maxima at the nutricline, and then decrease to low values in deep  
 390 layers. However, the random errors associated with individual cruise observations for  
 391  $\text{Si}(\text{OH})_4$  display no evident vertical pattern. Horizontally, we paid particular attention  
 392 to surface waters due to their greatest concentration gradients. The horizontal  
 393 distribution shows that the errors are small in the western NPSG (a nutrient-depleted  
 394 region) but are large in the subarctic gyre and close to the equatorial regions (nutrient-  
 395 replete regions; Figs. S8-S11). Here, we particularly examined the nutrient  
 396 reconstruction errors in the oligotrophic NPSG. The oligotrophic regimes are defined  
 397 as regions where  $\text{NO}_3^-$ ,  $\text{NO}_2^-$ , DIP, and  $\text{Si}(\text{OH})_4$  concentrations are  $<0.2$ ,  $<0.2$ ,  $<0.2$ ,  
 398 and  $<5.0 \mu\text{mol kg}^{-1}$ , respectively. As shown in Table 4, the reconstruction errors in these  
 399 regimes are  $<0.574$ ,  $<0.056$ ,  $<0.084$ , and  $<1.88 \mu\text{mol kg}^{-1}$  for  $\text{NO}_3^-$ ,  $\text{NO}_2^-$ , DIP, and

400 Si(OH)<sub>4</sub>, respectively, which are evidently lower than the overall RMSEs for the entire  
 401 North Pacific (Table 3). Among these models, the RF generally performs the best  
 402 compared to the others. This confirms that absolute errors decrease in oligotrophic  
 403 regimes. Since the number of summer observations is up to three times greater than that  
 404 in winter and spring, we further examined the seasonal variation of errors. Overall, no  
 405 evident seasonal variations are displayed. Only in the case of random cruise selection  
 406 was the NO<sub>3</sub><sup>-</sup> error shown to be greater in spring (March to May) than in other seasons  
 407 (Fig. S12). For other cases and nutrients, seasonal variation in error was not evident.  
 408 On a decadal timescale, the reconstruction errors display a slight decreasing trend,  
 409 particularly for DIP, from 1973 to 2020 (Fig. S13), implying that the errors might be  
 410 smaller in recent decades than in previous ones.

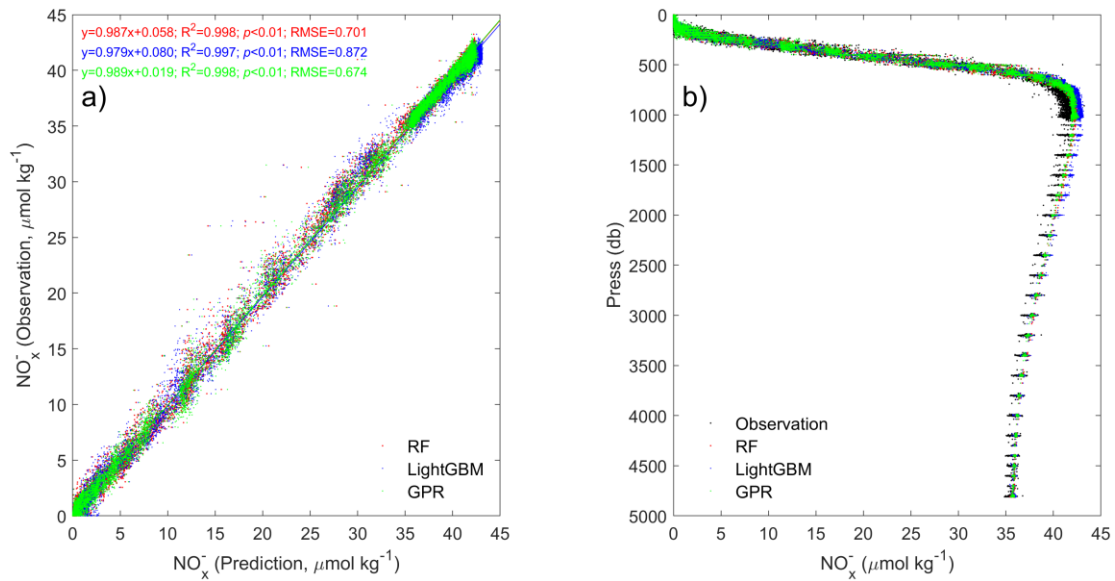
411 Table 4 The Root Mean Squared Errors of nutrient reconstruction from different error  
 412 evaluation strategies in surface oligotrophic regimes (unit:  $\mu\text{mol kg}^{-1}$ ).

Data selection strategy	NO <sub>x</sub> <sup>-</sup>			NO <sub>2</sub> <sup>-</sup>			DIP			Si(OH) <sub>4</sub>		
	RF	Light GBM	GPR	RF	Light GBM	GPR	RF	Light GBM	GPR	RF	Light GBM	GP R
Sample random	0.290	0.567	0.444	0.018	0.035	0.048	0.028	0.042	0.039	1.19	0.90	1.30
Station random	0.303	0.457	0.474	0.030	0.030	0.043	0.036	0.045	0.043	1.24	1.51	1.51
Cruise random	0.378	0.457	0.574	0.030	0.029	0.056	0.075	0.077	0.084	1.85	1.88	1.75

413

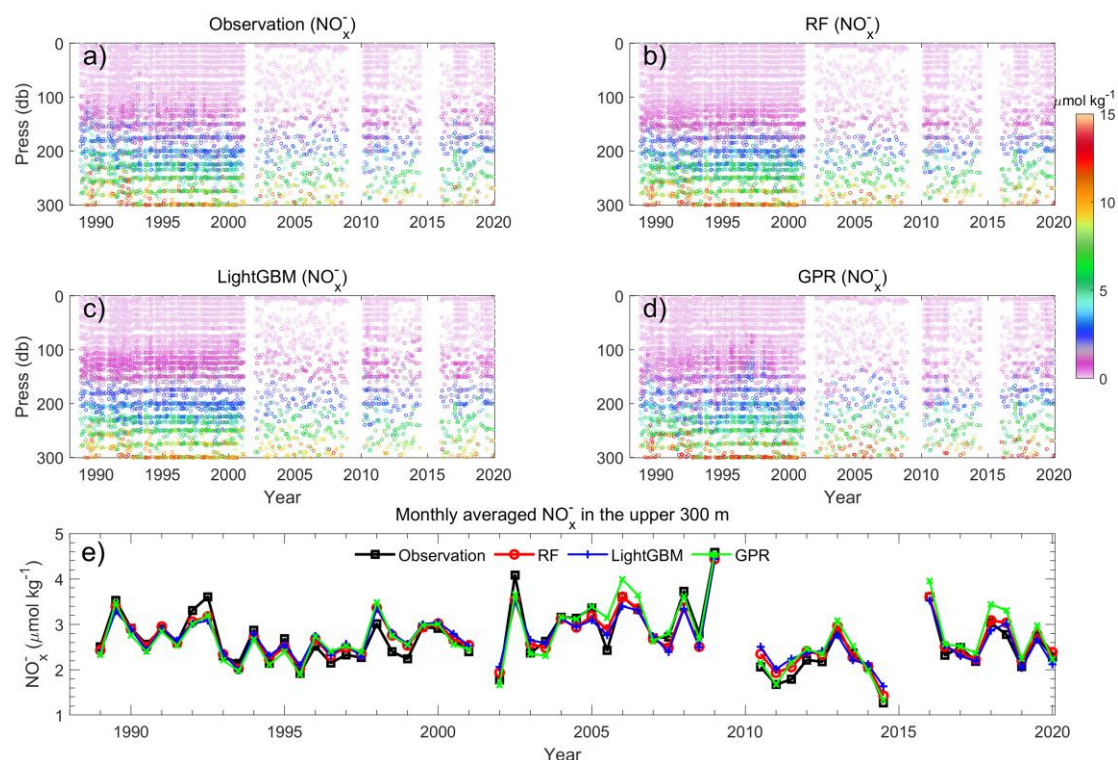
414 A fourth validation step assessed the model's temporal performance at Station  
 415 ALOHA (Error 4; Fig. 6b). To test this, we withheld all observations from ALOHA  
 416 (which, since 1988, represent 8.52%, 8.45%, and 8.11% of the total Si(OH)<sub>4</sub>, NO<sub>x</sub><sup>-</sup>, and  
 417 DIP records, respectively) from model training. We then reconstructed nutrient  
 418 concentrations using space, time, and water-type predictors at Station ALOHA. NO<sub>2</sub><sup>-</sup>  
 419 was excluded due to insufficient observations. For NO<sub>x</sub><sup>-</sup>, the regression slopes between  
 420 reconstruction and observations were 0.99, 0.98, and 0.99, with RMSEs of 0.701, 0.842,  
 421 and 0.674  $\mu\text{mol kg}^{-1}$  for RF, LightGBM, and GPR, respectively; R<sup>2</sup> values exceeded  
 422 0.997 for all models (Fig. 8a). RF and GPR slightly outperformed LightGBM. All  
 423 models accurately reproduced the NO<sub>x</sub><sup>-</sup> profiles (Fig. 8b). The reconstruction errors for  
 424 DIP were 0.066, 0.079, and 0.064  $\mu\text{mol kg}^{-1}$  for RF, LightGBM, and GPR, respectively.

425 The corresponding errors for  $\text{Si}(\text{OH})_4$  were 2.13, 2.48, and 2.32  $\mu\text{mol kg}^{-1}$  (Table 3,  
426 Figs. S14–S15).



427  
428 **Figure 8.** Validating the reconstructed nutrient concentrations at Station ALOHA. a)  
429 Reconstructed  $\text{NO}_3^- + \text{NO}_2^-$  ( $\text{NO}_x^-$ ) vs. observations: Random Forest (RF; red dots),  
430 LightGBM (blue dots), and Gaussian Process Regression (GPR; green dots). b) Profiles  
431 of observed (black dots) and reconstructed  $\text{NO}_x^-$  from RF (red dots), LightGBM (blue  
432 dots), and GPR (green dots).

433  
434 Since the variations of nutrients primarily occur in the upper water column, we  
435 focused on the nutrient reconstruction in the upper 300 m at Station ALOHA. Overall,  
436 the models reproduced the profiles of  $\text{NO}_x^-$  from 1988 to 2021 well (Fig. 9a-d). The  
437 reconstruction errors were low at the surface and increased with depth, with most of the  
438 values  $<3.0 \mu\text{mol kg}^{-1}$  (Fig. S16a-d). To evaluate models' ability to reconstruct nutrient  
439 variations in time, the nutrient concentrations were averaged monthly over the upper  
440 300 m. As compared to observations, RF, LightGBM, and GPR all well reconstructed  
441 the interannual variations of  $\text{NO}_x^-$  with most of the absolute errors  $<0.5 \mu\text{mol kg}^{-1}$  (Figs.  
442 9e and S16e) at Station ALOHA. Similarly, the validation of DIP and  $\text{Si}(\text{OH})_4$  are  
443 shown in Figs. S17-S20.



444

445 **Figure 9.** Temporal variations of NO<sub>x</sub><sup>-</sup> concentrations in the upper 300 m at Station  
 446 ALOHA from 1988 to 2021 for observed (a) and reconstructed NO<sub>x</sub><sup>-</sup> by Random Forest  
 447 (RF; b), LightGBM (c), and Gaussian Process Regression (GPR; d). (e) Time series of  
 448 monthly averaged NO<sub>x</sub><sup>-</sup> concentrations in the upper 300 m from observations, and  
 449 reconstructions by RF, LightGBM, and GPR.

450

451 A fifth validation step evaluates the models' reconstruction for the period before 1970  
 452 (Error 5; Fig. 6c). This is necessary because the training data (CCHDO) spans 1973–  
 453 2022, while the reconstructions are extrapolated back to 1895. We argue that this  
 454 extrapolation should be reasonable because the variations of temperature-salinity-  
 455 nutrient relationships in the ocean's interior might be small over the past century,  
 456 providing a basis for temporal extrapolation. First, the residence time of nitrogen in  
 457 deep and intermediate waters can be up to 2000 years in the North Pacific. Consequently,  
 458 the imprint of centennial-scale change on nutrient inventories is attenuated. Second, the  
 459 long-term variations of nutrient concentrations are not evident within our core training  
 460 period (1973–2022; Figs. 9e and 17). Finally, the mean nutrient profiles derived from  
 461 the 1920-1970 and 1973-2022 periods are not evidently different in the central North  
 462 Pacific (Fig. S21). Therefore, while the North Pacific may experience long-term

463 variability, it might be masked by the reconstruction error, and the use of hydrographic  
464 properties as predictors for nutrients is justified for historical reconstructions.

465 However, when assessing the reconstruction errors before 1970, we first consider  
466 data quality issues. Prior to the standardization of modern oceanographic methods,  
467 nutrient measurements—particularly from earlier decades—were subject to greater  
468 analytical errors, inconsistent sampling protocols, and varied determination techniques.  
469 The data quality concern is evident in the sporadic and sometimes physically  
470 implausible deep nutrient profiles found in WOD for that era (Fig. S22). This is also  
471 the primary reason that nutrient data pre-1973 collected from sources like the OSD from  
472 WOD were not incorporate into model training. To evaluate data quality in earlier  
473 decades, we selected five specific years with more abundant observations: 1929, 1947,  
474 1953, 1958, and 1966 (Fig. S23). After applying the same quality-control criteria  
475 outlined in Section 3.1, we used the historical hydrographic data (temperature and  
476 salinity) from those years to predict nutrient concentrations. A total of 52,277, 119,137,  
477 284,472, and 193,339 data points were collected for  $\text{NO}_3^-$ ,  $\text{NO}_2^-$ , DIP, and  $\text{Si}(\text{OH})_4$ ,  
478 respectively, after QC. The comparison between these predictions and the quality-  
479 controlled observations yields the prediction errors for the pre-1970 period (Fig. 6c).  
480 The RMSEs from different models suggested values  $<5.7$ ,  $<0.40$ , and  $<22.9 \mu\text{mol kg}^{-1}$   
481 for  $\text{NO}_3^-$ , DIP, and  $\text{Si}(\text{OH})_4$ , respectively (Figs. S24–S26), which are much larger than  
482 the corresponding errors for the period after 1970. We recommend that these values be  
483 considered a conservative estimate of the upper error bound, as they incorporate both  
484 nutrient observations and prediction errors. In addition, the hydrographic data are also  
485 less reliable in the earlier period. Thus, we acknowledge that reconstruction errors are  
486 likely higher for the pre-1973 period, and the error estimated here should be considered  
487 as a "best estimate" with quantified uncertainties, and encourage users to consider these  
488 error bounds when applying the dataset to early twentieth-century conditions.

489

### 490 **3.2 Reconstructed nutrients**

491 The final reconstructed nutrient dataset aligns with the spatiotemporal coverage of  
492 the quality-controlled WOD hydrographic dataset, comprising 472,652,680 data points  
493 for each nutrient ( $\text{NO}_x^-$ ,  $\text{NO}_2^-$ , DIP, and  $\text{Si}(\text{OH})_4$ ) from 1,920,634 stations across 35,744  
494 cruises, spanning from 1895 to 2024 (Table 2). Most data points are located above 2,000  
495 m, with fewer observations at greater depths due to hydrographic platform limitations.

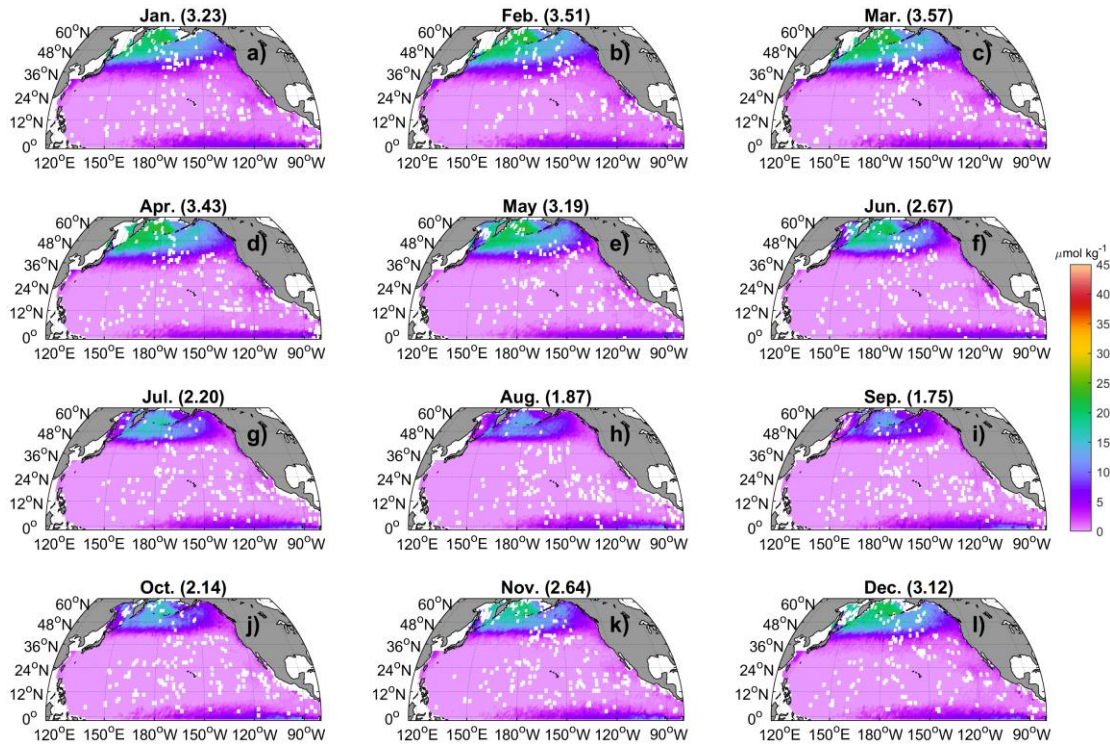
496 It is important to clarify the nature of the reconstructed dataset, which is  
497 fundamentally different from gridded products. This product provides nutrient  
498 concentrations linked to each hydrographic observations: nutrient values are  
499 reconstructed precisely at the locations, depths, and times of original hydrographic  
500 observations (sourced from WOD) where direct nutrient measurements might be  
501 unavailable or of poor quality. This approach yields a point-wise dataset that aligns with  
502 the original hydrographic observations, rather than a spatially or temporally  
503 interpolated field—an important distinction for users interpreting and applying the data.

### 504 **3.3 Climatology of nutrient distributions**

505 To evaluate the reliability of our product, we binned and averaged the predicted  
506 nutrients within  $1^\circ \times 1^\circ$  grid cells for each month to produce a monthly climatology. This  
507 climatology represents a mean field that depends heavily on the spatiotemporal  
508 distribution of the underlying data and may be influenced by uneven data sampling.  
509 This reconstructed climatology was compared with the World Ocean Atlas 2023  
510 (WOA23), which is derived from quality-controlled and objectively analyzed  
511 observational data. Since the large-scale patterns of  $\text{NO}_3^-$ , DIP, and  $\text{Si}(\text{OH})_4$  are similar  
512 among different models (Figs. 10–13, S27–S36), we focus on  $\text{NO}_3^-$  reconstructed by  
513 the RF model in this section unless stated otherwise.

514 Figs. 10–13 present the monthly climatology of  $\text{NO}_x^-$  at 5 m, 100 m, 500 m, and  
515 1,000 m in the North Pacific. At 5 m, the reconstructed  $\text{NO}_x^-$  accurately captures the  
516 established spatial patterns, with elevated concentrations in the subpolar gyre, Bering  
517 Sea, and equatorial regions, and depleted concentrations in the NPSG (Fig. 10).  
518 Seasonally, the basin-averaged surface  $\text{NO}_x^-$  concentrations display the highest value  
519 of  $3.50 \mu\text{mol kg}^{-1}$  in March, in contrast to the lowest value of  $1.82 \mu\text{mol kg}^{-1}$  in

520 September. These results agree with Yasunaka et al. (2014, 2021), who, using extensive  
 521 surface nutrient observations (up to 14,000 for nitrate) in the North Pacific, reported  
 522 similar spatial and seasonal patterns.

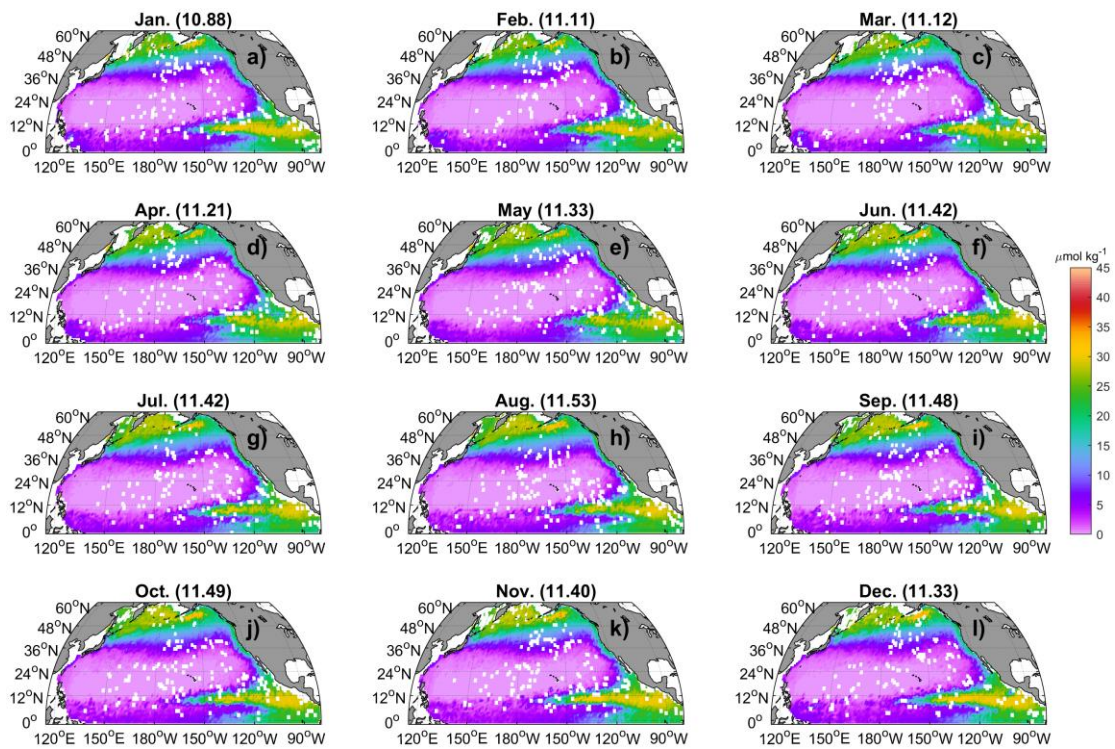


523 **Figure 10.** The monthly climatology of  $\text{NO}_x^-$  at 5 m in the North Pacific. Data are  
 524 binned and averaged within  $1 \times 1^\circ$  grid cells. The values in the title represent the spatial  
 525 mean values.  
 526

527

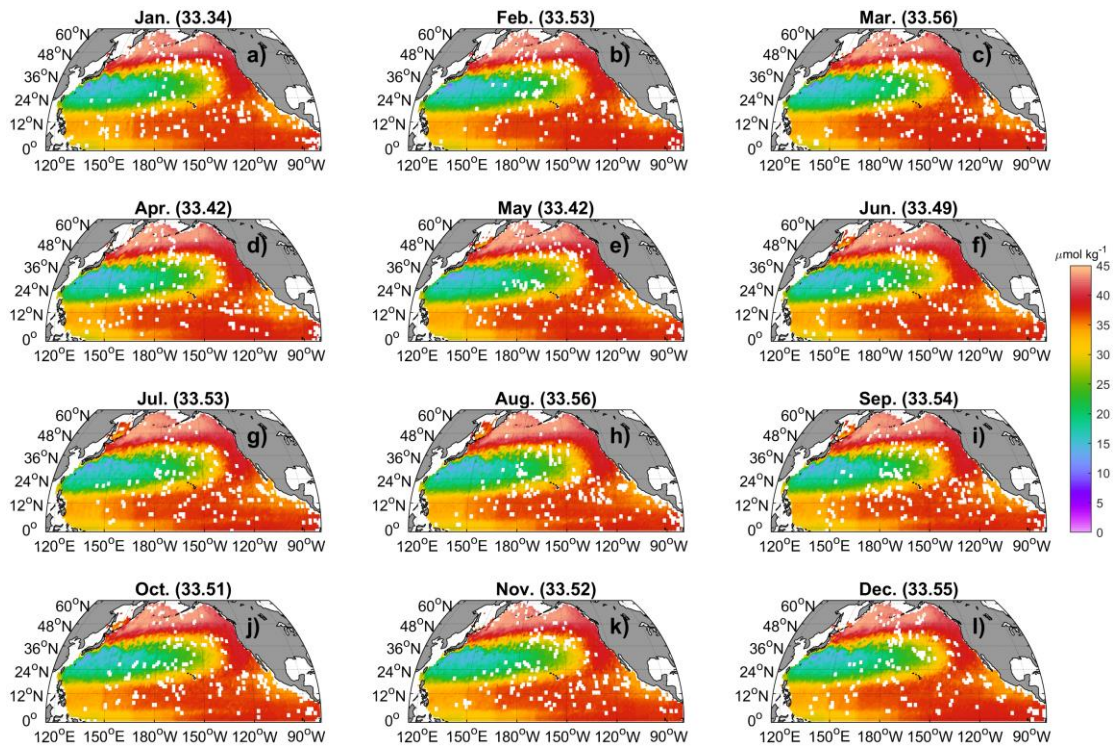
528 At 100 m,  $\text{NO}_x^-$  concentrations are elevated particularly in the subarctic gyre, north  
 529 of the Equator, and the eastern North Pacific, while the central regions, particularly the  
 530 NPSG, exhibit lower values. At 500 m,  $\text{NO}_x^-$  concentrations display patterns similar to  
 531 those at 100 m, except that the  $\text{NO}_x^-$  concentrations in the western NPSG are evidently  
 532 lower than those in other regions (Fig. 13). At 1000 m, concentrations in the  
 533 southwestern North Pacific Ocean are markedly lower than those in other regions (Fig.  
 534 12). Below 100 m depth, seasonal variability in  $\text{NO}_x^-$  is minimal (Figs. 11–13). These  
 535 results display patterns similar to WOA23 (Figs. S36–S44). The differences between  
 536 the averaged values of these two climatologies are generally  $<0.7 \mu\text{mol kg}^{-1}$  at the  
 537 surface and  $<1.5 \mu\text{mol kg}^{-1}$  at 100 m and 500 m. The maximum differences are found

538 in July at a depth of 500 m (Figs. 13g and S38g). In that month and layer, WOA23  
 539 shows a notably low mean  $\text{NO}_3^-$  value ( $31.94 \mu\text{mol kg}^{-1}$ ) compared to its values in other  
 540 months ( $33.15$  to  $34.64 \mu\text{mol kg}^{-1}$ ; Fig. S38) and compared to our climatology ( $33.34$   
 541 to  $33.56 \mu\text{mol kg}^{-1}$ ; Fig. 13). This discrepancy arises because the WOA23 climatology  
 542 for July features a pronounced low- $\text{NO}_3^-$  patch (down to  $20 \mu\text{mol kg}^{-1}$ ) within the  
 543 eastern subarctic gyre, surrounded by waters with concentrations of  $>35 \mu\text{mol kg}^{-1}$  (Fig.  
 544 S38g). These regional differences are clearly visible in the difference maps between the  
 545 two products (Figs. S45–S47). Generally, our reconstructions capture finer spatial detail,  
 546 exhibit less oversmoothing, and avoid artificial “bull’s-eye” patterns.



547  
 548 **Figure 11.** The monthly climatology of  $\text{NO}_x^-$  at 100 m in the North Pacific. Data are  
 549 binned and averaged within  $1 \times 1^\circ$  grid cells. The values in the title represent the spatial  
 550 mean values.

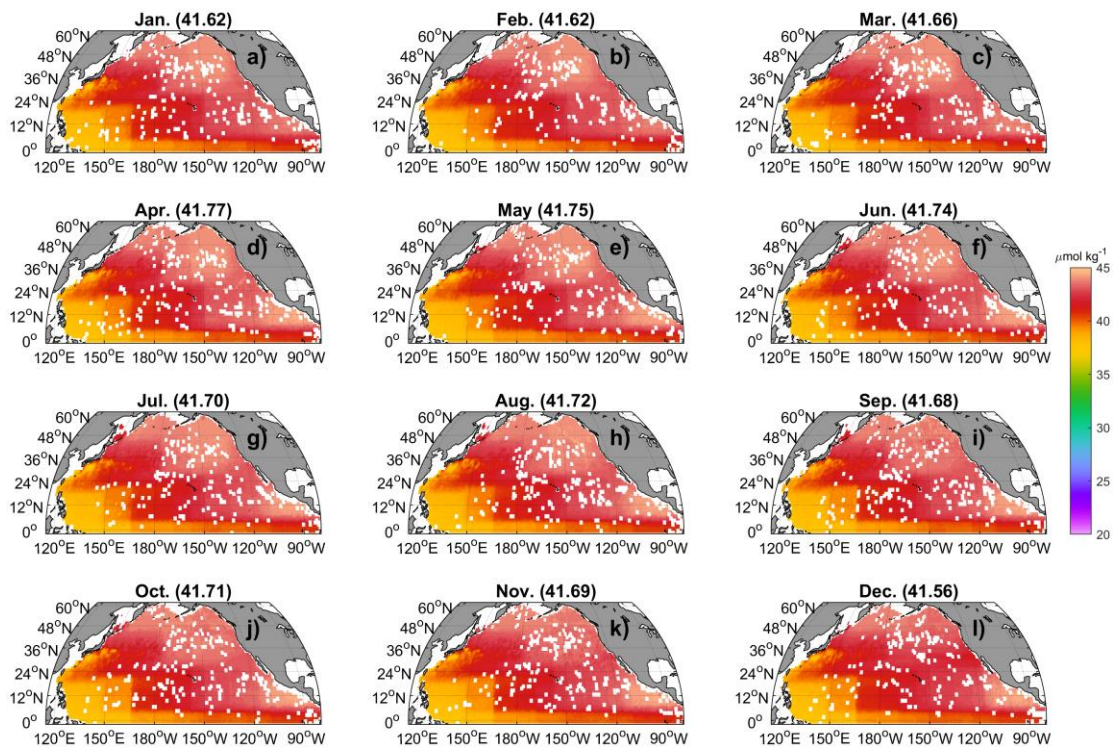
551



552

553 **Figure 12.** The monthly climatology of  $\text{NO}_x^-$  at 500 m in the North Pacific. Data are  
 554 binned and averaged within  $1 \times 1^\circ$  grid cells. The values in the title represent the spatial  
 555 mean values.

556

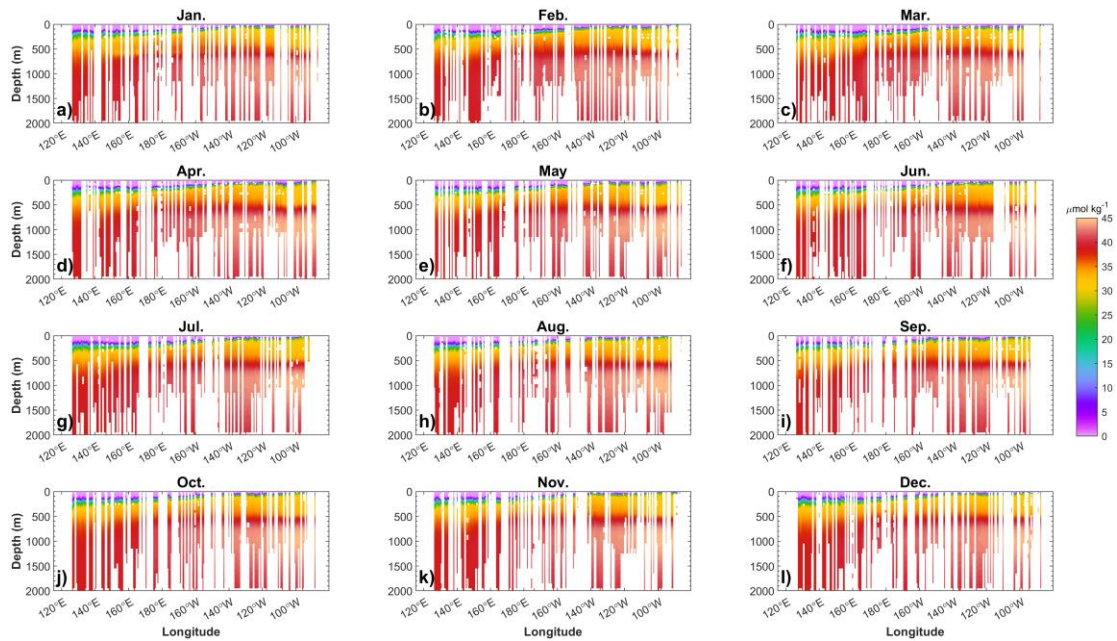


557

558 **Figure 13.** The monthly climatology of  $\text{NO}_x^-$  at 1000 m in the North Pacific. Data are  
 559 binned and averaged within  $1^\circ \times 1^\circ$  grid cells. The values in the title represent the spatial  
 560 mean values.

561

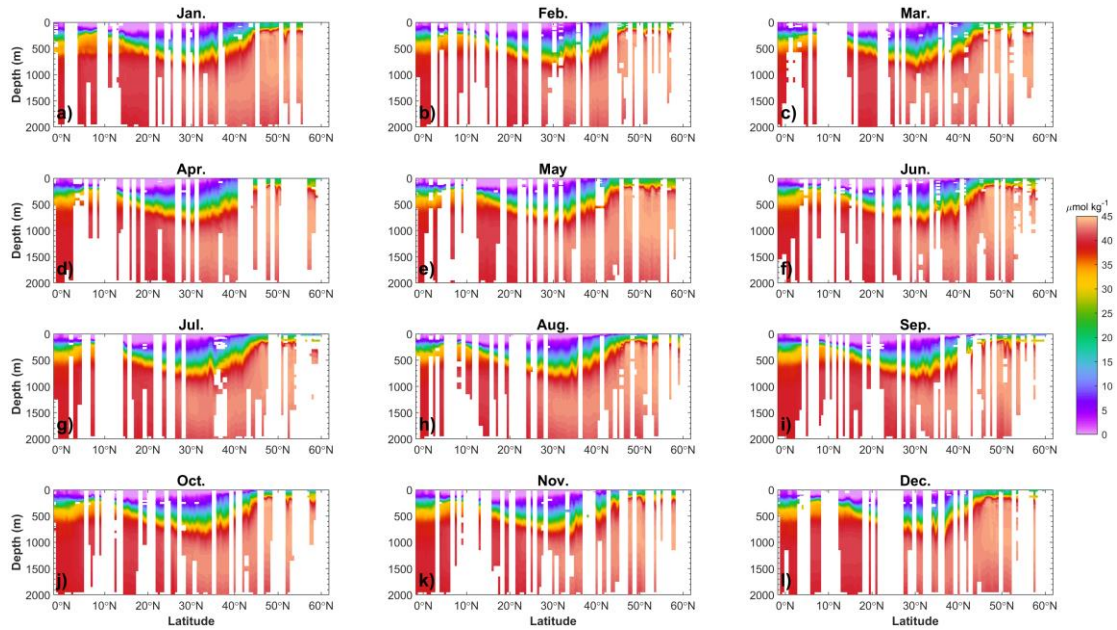
562 Sectional distributions of  $\text{NO}_x^-$  in the upper 2000 m along  $10^\circ$  N and  $180^\circ$  E were  
 563 used as examples to illustrate the vertical profile distributions of nutrients within the  
 564 North Pacific. At  $10^\circ$  N,  $\text{NO}_x^-$  concentrations increase from  $\sim 0.0 \mu\text{mol kg}^{-1}$  at the  
 565 surface to  $\sim 45.0 \mu\text{mol kg}^{-1}$  at  $\sim 1000$  m, followed by a decrease to  $\sim 38.0 \mu\text{mol kg}^{-1}$  at  
 566 2000 m.  $\text{NO}_x^-$  concentrations increase from west to the east in the North Pacific in the  
 567 upper 300 m (Fig. 14). At  $180^\circ$  E, in the upper 500 m, meridional  $\text{NO}_x^-$  concentrations  
 568 increase from the equator to the North Equatorial Current ( $\sim 10^\circ$  N), decline within the  
 569 subtropical gyre, and then increase toward the subarctic region (Fig. 15). Generally,  
 570 seasonal differences of  $\text{NO}_x^-$  concentrations along both sections are not evident.



571

572 **Figure 14.** Zonal and monthly climatology of  $\text{NO}_x^-$  in the upper 2000 m at  $10^\circ$  N in the  
 573 North Pacific. Data were binned and averaged within  $1^\circ \times 1^\circ$  grid cells.

574



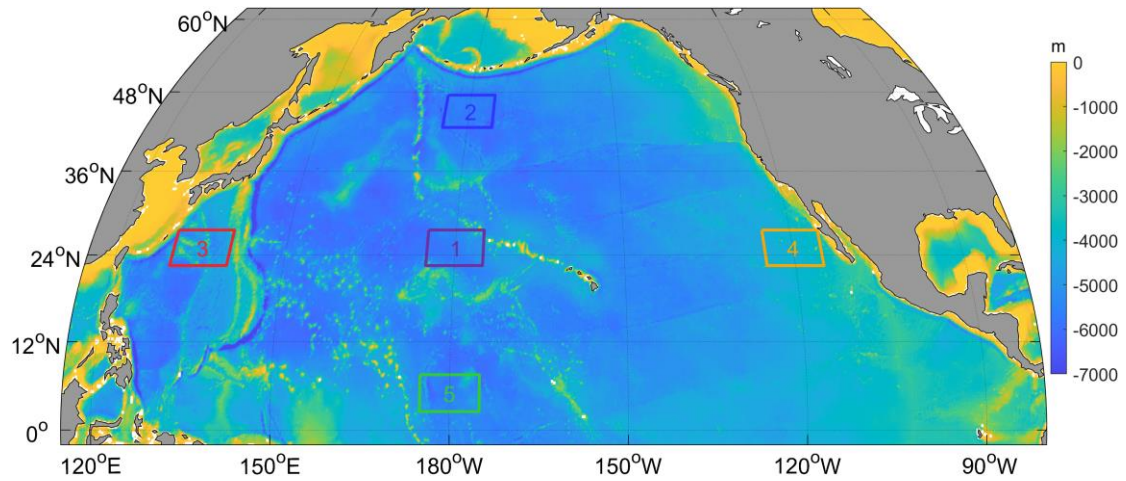
575

576 **Figure 15.** The monthly climatology of  $\text{NO}_x^-$  in the upper 2000 m at 170 °E section in  
 577 the North Pacific. Data were binned and averaged within  $1^\circ \times 1^\circ$  grid cells.

578

### 579 **3.4 Long-term variations of nutrients**

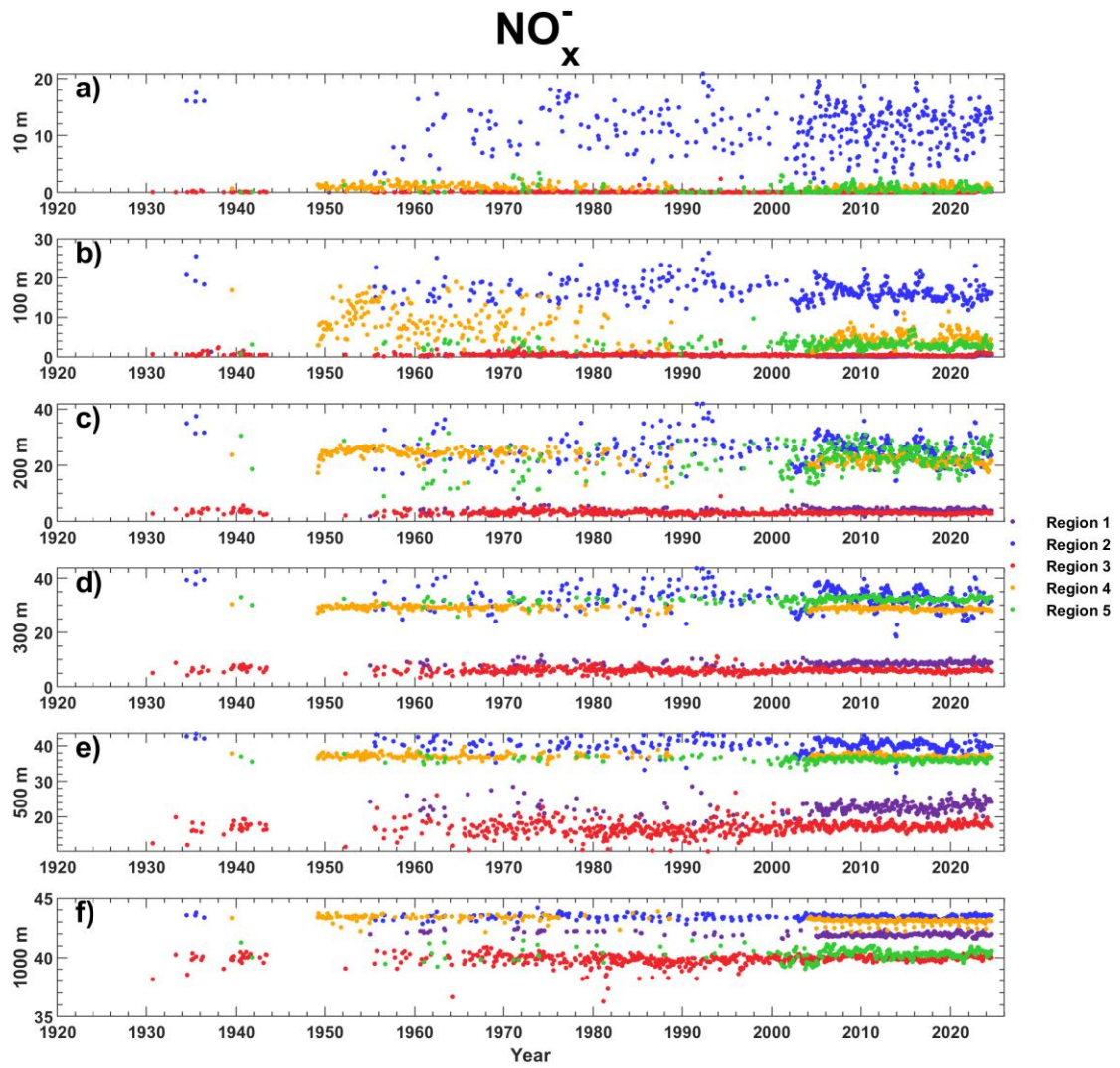
580 We present an initial analysis of long-term nutrient changes by examining five  
 581 representative regions in the North Pacific, covering the subarctic gyre, the subtropical  
 582 gyre, and equatorial areas (Fig. 16). The data are binned by region, month, and depth  
 583 (10 m, 100 m, 200 m, 300 m, 500 m, and 1000 m) for regions 1–5. As shown in Fig. 17,  
 584 these time series reveal notable interannual fluctuations of  $\text{NO}_3^-$  (with 2–5-year  
 585 oscillations), providing a first-order view of low-frequency variability captured by the  
 586 reconstruction. However, no evident long-term trend is found for nutrients. DIP and  
 587  $\text{Si}(\text{OH})_4$  display patterns similar to  $\text{NO}_3^-$  (Figs. S48–S49). In contrast, at depths of 200  
 588 m and 300 m,  $\text{NO}_2^-$  displays an increasing trend in the central NPSG and a decreasing  
 589 trend in the eastern NPSG during the 1970–2005 period (Fig. S50). More sophisticated  
 590 trend analyses and basin-scale integrations are promising avenues for future work based  
 591 on this newly reconstructed dataset.



592

593 **Figure 16.** Locations of five representative regions for analyzing long-term nutrient  
 594 variations.

595



596

597 **Figure 17.** Time series of reconstructed  $\text{NO}_3^-$  concentrations at 10 m (a), 100 m (b),  
598 200 m (c), 300 m (d), 500 m (e), and 1000 m (f) for regions 1–5 (see Fig. 16). Data  
599 were binned by depth and region and then averaged by month.

600

#### 601 **4 Data availability**

602 The database is available in a data repository (Du et al., 2025;  
603 <https://zenodo.org/records/17140658>). Although the reconstruction results from RF,  
604 LightGBM, and GPR are generally consistent, RF yields the best performance. To avoid  
605 redundancy and minimize storage requirements—given the large volume of the data  
606 files—only the nutrient data reconstructed by RF have been uploaded. Researchers may  
607 contact the corresponding authors to request the reconstructions generated by  
608 LightGBM and GPR.

609

#### 610 **5 Conclusion**

611 In this study, we applied rigorous quality control procedures to clean hydrographic  
612 and nutrient observations from CCHDO and WOD datasets. The cleaned CCHDO data  
613 were then used to train three machine-learning models to relate nutrient concentrations  
614 to spatial, temporal, and water-mass predictors. The models were applied to reconstruct  
615 nutrient concentrations from hydrographic observations collected from WOD, though  
616 most of which lack direct nutrient measurements. We assessed the model performance  
617 using four data-partition strategies, and found that all models reproduced held-out data  
618 with low RMSEs. RF and GPR slightly outperformed LightGBM. The application of  
619 these models to WOD hydrography yielded 472,652,680 reconstructed nutrient  
620 concentrations across 1,920,634 stations and 35,744 cruises, spanning from 1895 to  
621 2024. This represents a 2,127– to 2,393-fold increase compared to the original volume  
622 of CCHDO nutrient data. The reconstruction captured the spatial, seasonal, and  
623 interannual variations of water column nutrients in the North Pacific Ocean well.  
624 Compared to the WOA23 climatology, the reconstruction-based nutrient climatology  
625 exhibited more realistic spatial structures than WOA23. This high-quality and high-

626 resolution nutrient dataset adds historical nutrient estimation for locations and times  
627 with solely hydrographic measurements. The additionally potential application of this  
628 dataset include: 1) investigating nutrient transport and budget in the north Pacific; 2)  
629 spinning up and validating ocean biogeochemical models; 3) assessing long-term  
630 nutrient trends driven by anthropogenic forcing and climate change; 4) investigating  
631 nutrient stoichiometric changes and their ecological impacts under climate variability.  
632 Collectively, this resource facilitates advanced studies on marine biogeochemical  
633 cycles, ecosystem dynamics, and climate-nutrient interactions.

634

### 635 **Author contributions**

636 CD and XL designed the study and dataset. CD, SK, MD, ZC, DS, and XL conceived  
637 the project and secured the funding. CD, NZ, QL, HW and XL collected and processed  
638 the data, developed the code, and performed the analysis. SK, MD, ZC, and DS  
639 provided methodological guidance and advice. CD and NZ wrote the original draft. All  
640 authors reviewed, edited the manuscript.

641

### 642 **Competing interests**

643 The contact author has declared that none of the authors has any competing interests.

644

### 645 **Acknowledgements**

646 This study was funded by the National Natural Science Foundation of China (Grants  
647 42494885), National Key Research and Development Program of China  
648 (Grant 2023YFF0805001), This study was funded by the National Natural Science  
649 Foundation of China (Grants 42576215, 42494881), Innovational Fund for Scientific  
650 and Technological Personnel of Hainan Province (Grant KJRC2023B04), and Natural  
651 Science Foundation of Hainan Province (Grant 624MS037). We thank the CCHDO  
652 (<https://cchdo.ucsd.edu/>) and the WOD ([https://www.ncei.noaa.gov/products/world-](https://www.ncei.noaa.gov/products/world-ocean-database)  
653 [ocean-database](https://www.ncei.noaa.gov/products/world-ocean-database)) for providing the data used in this study. Special thanks are owed to all  
654 scientists involved in data collection, analysis, and management for these programs.

655

656 **Declaration of generative AI and AI-assisted technologies in the writing process:**

657 During the preparation of this work the authors used deepseek to check the spelling and  
658 grammar. After using this tool, the authors reviewed and edited the content as needed  
659 and take full responsibility for the content of the publication.

660

661 **References**

662 Arteaga, L., Pahlow, M., and Oschlies, A.: Global monthly sea surface nitrate fields  
663 estimated from remotely sensed sea surface temperature, chlorophyll, and  
664 modeled mixed layer depth, *Geophys. Res. Lett.*, 42, 1130–1138, 2015.

665 Ascani, F., Richards, K. J., Firing, E., Grant, S., Johnson, K. S., Jia, Y., et al.: Physical  
666 and biological controls of nitrate concentrations in the upper subtropical North  
667 Pacific Ocean, *Deep-Sea Res. Pt. II*, 93, 119–134, 2013.

668 Barone, B., Church, M. J., Dugenne, M., Hawco, N. J., Jahn, O., White, A. E., et al.:  
669 Biogeochemical dynamics in adjacent mesoscale eddies of opposite polarity,  
670 *Global Biogeochem. Cy.*, 36, e2021GB007115, 2022.

671 Benitez-Nelson, C. R., Bidigare, R. R., Dickey, T. D., Landry, M. R., Leonard, C. L., et  
672 al.: Mesoscale Eddies Drive Increased Silica Export in the Subtropical Pacific  
673 Ocean, *Science*, 316, 1017–1021, 2007.

674 Bidigare, R. R., Chai, F., Landry, M. R., Lukas, R., Hannides, C. C. S., Christensen, S.  
675 J., Karl, D. M., Shi, L., and Chao, Y.: Subtropical ocean ecosystem structure  
676 changes forced by North Pacific climate variations, *J. Plankton Res.*, 31, 1131–  
677 1139, 2009.

678 Bonnet, S., Caffin, M., Berthelot, H., and Moutin, T.: Hot spot of N<sub>2</sub> fixation in the  
679 western tropical South Pacific pleads for a spatial decoupling between N<sub>2</sub> fixation  
680 and denitrification, *Proc. Natl. Acad. Sci. USA*, 114, E2800–E2801, 2017.

681 Browning, T. J. and Moore, C. M.: Global analysis of ocean phytoplankton nutrient  
682 limitation reveals high prevalence of co-limitation, *Nat. Commun.*, 14, 5014, 2023.

683 Chelton, D. B., Schlax, M. G., Samelson, R. M., and de Szoeke, R. A.: Global  
684 observations of large oceanic eddies, *Geophys. Res. Lett.*, 34, L15606, 2007.

685 Chen, S., Hu, C., Barnes, B. B., Wanninkhof, R., Cai, W., Barbero, L., and Pierrot, D.:  
686 A machine learning approach to estimate surface ocean  $p\text{CO}_2$  from satellite  
687 measurements, *Remote Sens. Environ.*, 228, 203–226, 2019.

688 Chen, S., Meng, Y., Lin, S., Yu, Y., and Xi, J.: Estimation of sea surface nitrate from  
689 space: Current status and future potential, *Sci. Total Environ.*, 899, 165690, 2023.

690 Chen, S., Meng, Y., Shang, S., Zheng, M., Wang, Y., and Chai, F.: Remote estimates of  
691 sea surface nitrate and its trends from ocean color in the northwest Pacific, *J.*  
692 *Geophys. Res.*, 129, e2023JC019846, 2024.

693 Dai, M., Luo, Y., Achterberg, E. P., Browning, T. J., Cai, Y., Cao, Z., Chai, F., Chen, B.,  
694 Church, M. J., Ci, D., Du, C., Gao, K., Guo, X., Hu, Z., Kao, S., Laws, E. A., Lee,  
695 Z., Lin, H., Liu, Q., et al.: Upper Ocean biogeochemistry of the oligotrophic North  
696 Pacific subtropical gyre: From nutrient sources to carbon export, *Rev. Geophys.*,  
697 61, e2022RG000800, 2023.

698 Du, C., Zheng, N., Kao, S.-J., Dai, M., Cao, Z., Shi, D., Li, Q., Wang, H., and Li, X.:  
699 Validated temperature and salinity data, and reconstructed nutrient concentrations  
700 in the North Pacific (1895 - 2024). Zenodo, <https://zenodo.org/records/17451417>,  
701 2025.

702 Dave, A. C. and Lozier, M. S.: Local stratification control of marine productivity in the  
703 subtropical North Pacific, *J. Geophys. Res.*, 115, C12032, 2010.

704 Deutsch, C. and Weber, T.: Nutrient Ratios as a Tracer and Driver of Ocean  
705 Biogeochemistry, *Annu. Rev. Mar. Sci.*, 4, 113–138, 2012.

706 Dong, L., Qi, J., Yin, B., Zhi, H., Li, D., Yang, S., Wang, W., Cai, H., and Xie, B.:  
707 Reconstruction of subsurface salinity structure in the South China Sea using  
708 satellite observations: a LightGBM-Based Deep forest method, *Remote Sens.*, 14,  
709 3494, 2022.

710 Du, C., He, R., Liu, Z., Huang, T., Wang, L., Yuan, Z., Xu, Y., Wang, Z., and Dai, M.:  
711 Climatology of nutrient distributions in the South China Sea based on a large data  
712 set derived from a new algorithm, *Prog. Oceanogr.*, 195, 102586, 2021.

713 Dugdale, R. C., Morel, A., Bricaud, A., and Wilkerson, F. P.: Modeling new production  
714 in upwelling centers: A case study of modeling new production from remotely-  
715 sensed temperature and color, *J. Geophys. Res.*, 94, 18119–18132, 1989.

716 Eugster, O. and Gruber, N.: A probabilistic estimate of global marine N-fixation and  
717 denitrification, *Glob. Biogeochem. Cycles*, 26, GB4013, 2012.

718 Fuhr, M., Laukert, G., Yu, Y., Nürnberg, D., and Frank, M.: Tracing water mass mixing  
719 from the Equatorial to the North Pacific Ocean with dissolved neodymium  
720 isotopes and concentrations, *Front. Mar. Sci.*, 7, 603761, 2021.

721 Gan, M., Pan, S., Chen, Y., Cheng, C., Pan, H., and Zhu, X.: Application of the Machine  
722 Learning LightGBM model to the prediction of the water levels of the Lower  
723 Columbia River, *J. Mar. Sci. Eng.*, 9, 496, 2021.

724 Garcia, H. E., Boyer, T. P., Locarnini, R. A., Reagan, J. R., Mishonov, A. V., Baranova,  
725 O. K., Paver, C. R., Wang, Z., Bouchard, C. N., Cross, S. L., Seidov, D., and  
726 Dukhovskoy, D.: World Ocean Database 2023: User's Manual. A.V. Mishonov,  
727 Technical Ed., NOAA Atlas NESDIS, 98, 129 pp., 2024.

728 Goes, J. I., Saino, T., Oaku, H., and Jiang, D. L.: A Method for Estimating Sea Surface  
729 Nitrate Concentrations from Remotely Sensed SST and Chlorophyll - A Case  
730 Study for the North Pacific Ocean Using OCTS/ADEOS Data, *IEEE Trans. Geosci.*  
731 *Remote Sens.*, 37, 1633–1644, 1999.

732 Hu, C., Feng, L., and Guan, Q.: A machine learning approach to estimate surface  
733 chlorophyll *a* concentrations in global oceans from satellite measurements, *IEEE*  
734 *Trans. Geosci. Remote Sens.*, 59, 4590–4607, 2021.

735 Huang, Y., Nicholson, D., Huang, B., and Cassar, N.: Global estimates of marine gross  
736 primary production based on machine learning upscaling of field observations,  
737 *Global Biogeochem. Cy.*, 35, e2020GB006718, 2021.

738 Huang, Y., Tagliabue, A., and Cassar, N.: Data-Driven Modeling of Dissolved Iron in  
739 the Global Ocean, *Front. Mar. Sci.*, 9, 837183, 2022.

740 Kamykowski, D., Zentara, S.-J., Morrison, J. M., and Switzer, A. C.: Dynamic global  
741 patterns of nitrate, phosphate, silicate, and iron availability and phytoplankton  
742 community composition from remote sensing data, *Global Biogeochem. Cy.*, 16,  
743 1077, 2002.

744 Kamykowski, D.: A preliminary model of the relationship between temperature and  
745 plant nutrients in the upper ocean, *Deep-Sea Res.*, 34, 1067–1079, 1987.

746 Kamykowski, D.: Estimating upper ocean phosphate concentrations using ARGO float  
747 temperature profiles, *Deep-Sea Res. Pt. I*, 55, 1580–1589, 2008.

748 Karl, D. M. and Church, M. J.: Ecosystem structure and dynamics in the North Pacific  
749 Subtropical Gyre: new views of an old ocean, *Ecosystems*, 20, 433–457, 2017.

750 Karl, D. M., Letelier, R. M., Bidigare, R. R., Björkman, K. M., Church, M. J., Dore, J.  
751 E., and White, A. E.: Seasonal-to-decadal scale variability in primary production  
752 and particulate matter export at Station ALOHA, *Prog. Oceanogr.*, 195, 102563,  
753 2021.

754 Ke, G., Meng, Q., Finley, T., Wang, T., Chen, W., Ma, W., Ye, Q., and Liu, T.-Y.:  
755 Lightgbm: A highly efficient gradient boosting decision tree, *Adv. Neural Inf.*  
756 *Process. Syst.*, 30, 3147–3155, 2017.

757 Lee, G. S., Lee, J. H., and Cho, H. Y.: Spatiotemporal estimation of nutrient data from  
758 the northwest pacific and east Asian seas, *Sci. Data*, 10, 2023.

759 Liaw, A. and Wiener, M.: Classification and regression by randomForest, *R News*, 2,  
760 18–22, 2002.

761 Lipschultz, F., Bates, N. R., Carlson, C. A., and Hansell, D. A.: New production in the  
762 Sargasso Sea: History and current status, *Global Biogeochem. Cy.*, 16, 1001, 2002.

763 Liu, H., Lin, L., Wang, Y., Du, L., Wang, S., Zhou, P., Yu, Y., Gong, X., and Lu, X.:  
764 Reconstruction of Monthly Surface Nutrient Concentrations in the Yellow and  
765 Bohai Seas from 2003–2019 Using Machine Learning, *Remote Sens.*, 14, 5021,  
766 2022.

767 Madani, N., Parazoo, N. C., Manizza, M., Chatterjee, A., Carroll, D., Menemenlis, D.,  
768 Fouest, V. L., Matsuoka, A., Luis, K. M., Serra-Pompei, C., and Miller, C. E.: A  
769 machine learning approach to produce a continuous Solar-Induced chlorophyll  
770 fluorescence over the Arctic Ocean, *J. Geophys. Res. Machine Learn. Comput.*, 1,  
771 2024.

772 Martino, M., Hamilton, D. S., Baker, A. R., Jickells, T., Bromley, T., Nojiri, Y., Quack,  
773 B., and Boyd, P. W.: Western Pacific atmospheric nutrient deposition fluxes, their  
774 impact on surface ocean productivity, *Glob. Biogeochem. Cycles*, 28, 712–728,  
775 2014.

776 Mishonov, A. V., Boyer, T. P., Baranova, O. K., Bouchard, C. N., Cross, S. L., Garcia,  
777 H. E., Locarnini, R. A., Paver, C. R., Reagan, J. R., Wang, Z., Seidov, D., Grodsky,  
778 A. I., and Beauchamp, J. G.: *World Ocean Database 2023*, C. Bouchard, Technical  
779 Ed., NOAA Atlas NESDIS, 97, 2024.

780 Moore, C. M., Mills, M. M., Arrigo, K. R., Berman - Frank, I., Bopp, L., Boyd, P. W.,  
781 Galbraith, E. D., Geider, R. J., Guieu, C., Jaccard, S. L., Jickells, T. D., Lenton, T.  
782 M., Mahowald, N. M., Marañón, E., Marinov, I., Moore, J. K., Nakatsuka, T.,  
783 Oschlies, A., Saito, M. A., Thingstad, T., Tsuda, A., and Ulloa, O.: Processes and  
784 patterns of oceanic nutrient limitation, *Nat. Geosci.*, 6, 701–710, 2013.

785 Mozejko, J. and Gniot, R.: Application of Neural Networks for the Prediction of Total  
786 Phosphorus Concentrations in Surface Waters, *Pol. J. Environ. Stud.*, 17, 363–368,  
787 2008.

788 Palacios, D. M., Hazen, E. L., Schroeder, I. D., and Bograd, S. J.: Modeling the  
789 temperature-nitrate relationship in the coastal upwelling domain of the California  
790 Current, *J. Geophys. Res.*, 118, 1–17, 2013.

791 Qi, J., Yu, Y., Yao, X., Yuan, G., and Gao, H.: Dry deposition fluxes of inorganic  
792 nitrogen and phosphorus in atmospheric aerosols over the Marginal Seas and  
793 Northwest Pacific, *Atmos. Res.*, 245, 105076, 2020.

794 Reagan, J. R., Boyer, T. P., García, H. E., Locarnini, R. A., Baranova, O. K., Bouchard,  
795 C., Cross, S. L., Mishonov, A. V., Paver, C. R., Seidov, D., Wang, Z., and

796 Dukhovskoy, D.: World Ocean Atlas 2023, NOAA National Centers for  
797 Environmental Information, Dataset, NCEI Accession 0270533, 2024.

798 Sarangi, P. K., Thangaradjou, T., Kumar, A. S., and Balasubramanian, T.: Development  
799 of nitrate algorithm for the southwest bay of bengal water and its implication using  
800 remote sensing satellite datasets, *IEEE J. Sel. Top. Appl. Earth Obs. Remote Sens.*,  
801 4, 983–991, 2011.

802 Sigman, D. M. and Hain, M. P.: The Biological Productivity of the Ocean, *Nat. Educ.*  
803 *Knowl.*, 3, 21, 2012.

804 Steinhoff, T., Friedrich, T., Hartman, S. E., Oeschies, A., Wallace, D. W. R., and  
805 Körtzinger, A.: Estimating mixed layer nitrate in the North Atlantic Ocean,  
806 *Biogeosciences*, 7, 795–807, 2010.

807 Su, H., Lu, X., Chen, Z., Zhang, H., Lu, W., and Wu, W.: Estimating Coastal  
808 Chlorophyll-A Concentration from Time-Series OLCI Data Based on Machine  
809 Learning, *Remote Sens.*, 13, 576, 2021.

810 Sundararaman, H. K. K. and Shanmugam, P.: Estimates of the global ocean surface  
811 dissolved oxygen and macronutrients from satellite data, *Remote Sens. Environ.*,  
812 311, 114243, 2024.

813 Switzer, A. C., Kamykowski, D., and Zentara, S.-J.: Mapping nitrate in the global ocean  
814 using remotely sensed sea surface temperature, *J. Geophys. Res.*, 108, 345–359,  
815 2003.

816 Talley, L. D., Pickard, G. L., Emery, W. J., and Swift, J. H.: *Descriptive Physical*  
817 *Oceanography, An Introduction, Sixth Edition*, Academic Press, 350–362 pp.,  
818 2011.

819 Wang, C., Su, B., Sun, J., Hu, X., and Liu, J.: A regional ocean database for the Coastal  
820 China Sea. *Sci Data*, 12, 1550, 2025.

821 Wang, L., Xu, Z., Gong, X., Zhang, P., Hao, Z., You, J., Zhao, X., and Guo, X.:  
822 Estimation of nitrate concentration and its distribution in the northwestern Pacific  
823 Ocean by a deep neural network model, *Deep Sea Res. I*, 195, 104005, 2023.

824 Wang, Z., Wang, G., Guo, X., Hu, J., and Dai, M.: Reconstruction of High-Resolution  
825 Sea Surface Salinity over 2003–2020 in the South China Sea Using the Machine  
826 Learning Algorithm LightGBM Model, *Remote Sens.*, 14, 6147, 2022.

827 Yang, G. G., Wang, Q., Feng, J., He, L., Li, R., Lu, W., Liao, E., and Lai, Z.: Can three-  
828 dimensional nitrate structure be reconstructed from surface information with  
829 artificial intelligence? – A proof-of-concept study, *Sci. Total Environ.*, 924,  
830 171365, 2024.

831 Yasunaka, S., Mitsudera, H., Whitney, F., and Nakaoka, S.: Nutrient and dissolved  
832 inorganic carbon variability in the North Pacific, *J. Oceanogr.*, 77, 3–16, 2021.

833 Yasunaka, S., Nojiri, Y., Nakaoka, S., Ono, T., Whitney, F. A., and Telszewski, M.:  
834 Mapping of sea surface nutrients in the North Pacific: Basin-wide distribution and  
835 seasonal to interannual variability, *J. Geophys. Res. Oceans*, 119, 7756–7771,  
836 2014.

837 Yasunaka, S., Ono, T., Nojiri, Y., Whitney, F. A., Wada, C., Murata, A., Nakaoka, S.,  
838 and Hosoda, S.: Long-term variability of surface nutrient concentrations in the  
839 North Pacific, *Geophys. Res. Lett.*, 43, 3389–3397, 2016.

840 Yu, X. R., Wen, Z., Jiang, R., Yang, J.-Y. T., Cao, Z., Hong, H., Zhou, Y., and Shi, D.:  
841 Assessing N<sub>2</sub> fixation flux and its controlling factors in the (sub)tropical western  
842 North Pacific through high-resolution observations, *Limnol. Oceanogr. Lett.*, 9,  
843 716 – 724, 2024.

844 Zhong, A., Wang, D., Gong, F., Zhu, W., Fu, D., Zheng, Z., Huang, J., He, X., and Bai,  
845 Y.: Remote sensing estimates of global sea surface nitrate: Methodology and  
846 validation, *Sci. Total Environ.*, 950, 175362, 2024.

847

848